2017

Performance analysis on Free-piston linear expander

Furkan Kodakoglu
University of North Florida

Suggested Citation

Kodakoglu, Furkan, "Performance analysis on Free-piston linear expander" (2017). *UNF Graduate Theses and Dissertations*. 766.
https://digitalcommons.unf.edu/etd/766

PERFORMANCE ANALYSIS ON FREE-PISTON LINEAR EXPANDER

by

Furkan Kodakoğlu

A thesis submitted to the Department of Mechanical Engineering

In partial fulfillment of the requirements for the degree of

Masters of Science in Mechanical Engineering

UNIVERSITY OF NORTH FLORIDA

COLLEGE OF COMPUTING, CONSTRUCTION, AND ENGINEERING

August, 2017

Certificate of Approval

The thesis “Performance analysis on free-piston linear expander” submitted by Furkan Kodakoğlu in partial fulfillment of the requirements for the degree of Master of Science in Mechanical Engineering has been

Approved by the thesis committee: **Date**

Dr. John Nuszkowski
Thesis Advisor and Committee Chairperson

Dr. Stephen Stagon

Dr. Gregory Thompson

Accepted for the School of Engineering:

Dr. Murat Tiryakioğlu
Director of the School

Accepted for the College of Computing, Engineering, and Construction:

Dr. Mark Tumeo
Dean of the College

Accepted for the University:

Dr. John Kantner
Dean of the Graduate School

Acknowledgements

First, I would like to express my deepest gratitude to my advisor Dr. John Nuszkowski for giving me the opportunity to work on this project under his supervision. I had a golden learning experience by benefiting from your professional knowledge, guidance and experimentalist skills throughout my study.

I am also grateful to Dr. Gregory Thompson and Dr. Stephen Stagon for their interests in this study and accepting to be on my thesis committee.

I would like to thank Dr. Murat Tiryakioğlu for his valuable and motivational support. His encouragement has given me a priceless power. My appreciation is extended to my friend Aygun Baltaci, a former electrical engineering student of UNF, for helping me through the adapting process from the beginning of my USA journey. I wish him great successes during his master's studies in the Technical University of Munich and after his graduation.

I would also like to thank Dr. Alexandra Schonning for keeping her door always open to me. In addition, a special thanks goes to the great staff of UNF, especially Jean Loos for giving me the chance to learn very useful skills in the machining stages of my study. She is an excellent teaching specialist.

The completion of this research project would not be possible without the constant support of my family. I thank my father and my mother for being my personal guidance and raising me to this day, and my brother for always being there whenever I need him.

Table of Contents

List of Figures

List of Tables

List of Abbreviations

AI	Analog Input
BDC	Bottom Dead Center
CHP	Combined Heat and Power
CO_2	Carbon Dioxide
COP	Coefficient of Performance
EMF	Electromotive Force
FPLE	Free-Piston Linear Expander
GND	Ground
GWP	Greenhouse Warming Potential
HCFC	Hydrochlorofluorocarbons
HFC	Hydrofluorocarbons
ID	Inner Diameter
LOE	Location of Expansion
MTOE	Million Tonnes of Oil Equivalent
OD	Outer Diameter
ODP	Ozone Depleting Potential
ORC	Organic Rankine Cycle
RMS	Root Mean Square
RO	Reverse Osmosis
RoHS	Restriction of Hazardous Substances
RPM	Revolution per Minute
SORC	Solar Organic Rankine Cycle
TDC	Top Dead Center
TEG	Thermoelectric Generator

List of Symbols

$\dot{S}_{gen}$	Entropy Generation
$\dot{W}_{e,avg}$	Average Electrical Power Output
$\dot{W}_{out,a}$	Rate of Actual Work Output
$\dot{W}_{out,s}$	Rate of Isentropic Work Output
$\dot{m}_a$	Mass Flow Rate of Air
E_{cv}	Total Internal Energy in Control Volume
m_{cv}	Mass in Control Volume
η_{Carnot}	Carnot Efficiency
$\dot{Q}$	Rate of Heat Transfer
R_a	Gas Constant of Air
R_{eq}	Equivalent Resistance
$T_{out,a}$	Exit Temperature in Actual Process
$T_{out,s}$	Exit Temperature in Isentropic Process
T_s	Temperature of Surroundings
$\dot{V}$	Volumetric Flow Rate
V_{RMS}	RMS Voltage
V_d	Displacement Volume
$\dot{W}$	Rate of Work
c_p	Specific Heat
$\dot{m}$	Mass Flow Rate
η_c	Mechanical-Electrical Conversion Efficiency
η_s	Isentropic Efficiency
ρ_a	Density of Air
ΔT	Temperature Gradient
ΔV	Voltage Differential
h	Enthalpy
$\mathrm{P}_{\mathrm{crit}}$	Critical Pressure
S	Entropy
T_0	Ambient Temperature
$\mathrm{T}_{\mathrm{crit}}$	Critical Temperature
T_{H}	Constant Temperature of High Heat Source
T_{L}	Constant Temperature of Low Heat Source
D	Diameter
I	Irreversibility
V	Velocity
f	Frequency
k	Specific Heat Ratio
n	Shaft Speed
t	Time
v	Tip Speed
z	Height Level
α	Seebeck Coefficient

λ	Volumetric Efficiency
σ	Standard Deviation

Abstract

The growing global demand for energy and environmental implications have created a need to further develop the current energy generation technologies (solar, wind, geothermal, etc.). Recovering energy from low grade energy sources such as waste heat is one of the methods for improving the performance of thermodynamic cycles. The objective of this work was to achieve long-term steady state operation of a Free-Piston Linear Expander (FPLE) and to compare the FPLE with the currently existing expander types for use in low temperature energy recovery systems. A previously designed FPLE with a single piston, two chambers, and linear alternator was studied and several modifications were applied on the sealing and over expansion. An experimental test bench was developed to measure the inlet and outlet temperatures, inlet and outlet pressures, flow rate, and voltage output. A method of thermodynamic analysis was developed by using the first and second law of thermodynamics with air as the working fluid. The experimental tests were designed to evaluate the performance of the FPLE with varying parameters of inlet air pressure, inlet air temperature, and electrical resistance. The initial and steady-state operation of the FPLE were successfully achieved. An uncertainty analysis was conducted on the measured values to determine the accuracies of the calculated parameters. The trends of several output parameters such as frequency, average root mean square (RMS) voltage, volumetric efficiency, electrical-mechanical conversion efficiency, isentropic efficiency, irreversibility, actual expander work, and electrical power were presented. Results showed that the maximum expander frequency was found to be 44.01 Hz and the frequency tended to increase as the inlet air pressure increased. The FPLE achieved the maximum isentropic efficiency of 21.5%, and produced maximum actual expander work and electrical work of 75.13 W and 3.302 W, respectively.

1 Introduction

A great amount of energy that the planet earth contains and “the unlimited” energy that the sun keeps providing shows the energy potential that can be reached. The human race has started to become more capable of using this potential in order to improve the quality of human life. However, “usable” energy has always been an essential need. Since the industrial revolution, the need for energy has been rapidly increasing mainly due to industrialization, and the changes in transportation and manufacturing processes around the world. In conjunction with this revolution, the power of heat was discovered and replaced the power need that was met by means of human- or/and animal-based methods. After the invention of the steam engine, by James Watt [1], in the 1800s and the technology developments that followed, society entered into a "technology era." This demand on technology that relies on mechanical or electrical power ensures the continued significance of the global energy supply.

Unfortunately, the vast majority of the growing global energy demand (81.6%) is met by fossil fuels [2]. Table 1.1 presents the share distribution of the world global energy demand by source. The combustion of the fossil fuels consisting of hydrocarbon components produces several pollutants such as carbon dioxide, sulfur dioxide, nitric oxides, carbon monoxide, and partly unburned particulates. These byproducts are responsible for several global threats, e.g. global warming, acid rain, ocean acidification, and environmental pollution that have hazardous effects for all living beings [3,23].

Table 1.1: World Primary Energy Demand by Source [2]

	MTOE	Percent %
Coal	3 773	28.9
Oil	4 108	31.4
Gas	2 787	21.3
Nuclear	674	5.2
Hydro	300	2.3
Bioenergy	1 300	9.9
Other renewables	127	1
Total	13 069	100

The percentages above do not represent the total amount of energy that is converted into usable power. The efficiency of power generation, at this point, becomes the crucial consideration. Efficiency is defined by the ratio of the energy obtained to the energy input and is usually expressed in percentages. As is the case with all processes, energy conversion from chemical to electrical power has inherent losses and limitations. Heat and friction losses can be considered as the main inherent losses. The Carnot efficiency, which is the theoretical maximum efficiency of any thermodynamic cycle, is one of the limitations.

The primary energy consumption of the U.S. is approximately 100 quadrillion [Btu] (approximately 2521 MTOE, or 1.06 X 10^{20} Joules) each year, and 20% of this total amount, 20 quadrillion Btu, is provided by coal. In addition to this, 92% of the coal source used in the U.S. is converted into electricity power [4]. The average conversion efficiency of the coal power plants operating in the U.S. is about 34% [5]. These facts indicate that

6.26 of the 18.4 quadrillion [Btu] of energy has been converted into electricity and the rest is released into the environment as waste energy in the U.S. each year. Power generation from other sources can be assumed to have a similar situation that results in waste energy.

Current global trends clearly show that the demand for fossil fuels will increase until 2035 [2], thereby forcing us to further develop current energy generation technologies. In this regard, efficiencies of the current thermodynamic cycle designs also need to be improved so that the dependence on the fossil fuels can be decreased. Low temperature heat recovery, in this case, has the potential to utilize the waste energy, thereby increasing the efficiency of the cycles and helping to reduce air pollution.

The purpose of this work was to investigate the potential of a new type of expander, the free-piston linear expander (FPLE), outlined by Henry B. Bonar [6]. It was also of interest to this work to design and build the FPLE to analyze the feasibility of the expander for advanced low temperature heat recovery systems.

2 Low Temperature Energy Recovery

The energy sources can be categorized by their grade and divided into three main categories, low temperature (<230 °C), medium temperature (230-650 °C), and high temperature (>650 °C) [7]. There are several methods to utilize the waste energy sources including the Carnot cycle, the Transcritical CO_2 cycle, the Kalina cycle, the Organic Rankine cycle (ORC), the Stirling engine and the thermoelectric generator (TEG). ORC, Transcritical CO_2 and Kalina cycles can be considered as modifications of the Rankine cycle. The Stirling engine is a closed reversible cycle that typically resembles the Carnot cycle. TEGs are devices working on the principle of the Seebeck effect and producing a voltage from a heat flux [8]. A cursory review and considerations of these methods and the expanders will be presented.

2.1 Carnot Cycle

The efficiency of any thermodynamic cycle is limited by the second law of thermodynamics. The low temperature energy recovery cycles are, therefore, limited by the Kelvin-Planck statement, which is best expressed as follows:

"It is impossible to construct a device that will operate in a cycle and produce no effect other than the raising of a weight and the exchange of heat with a single reservoir [3]."

Regarding the statement, the Carnot cycle expresses the maximum efficiency that any heat engine operating between two different, hot and cold, reservoirs can achieve as follows:

$$\eta_{Carnot} = 1 - \frac{T_L}{T_H}$$

where T_H is the constant temperature of the high temperature heat source and T_L is the constant temperature of the low temperature heat rejection sink. Therefore, the Carnot efficiency, achieved by assuming all the processes are reversible, clearly indicates that the maximum efficiency of any cycle only depends on the temperatures of the reservoirs. It is usually not possible to configure the temperature of rejection sink, but the temperature of the heat source may be pre-adjusted in order to increase the efficiency. Figure 2.1 presents the Carnot efficiency values as a function of heat source temperature (T_H) with the ambient temperature (T_0) value taken as a reference for the rejection sink temperature. It can be easily seen that the maximum efficiency that can be achieved acts quite sensitive under 700 °C, indicating that the low temperature energy recovery systems will have lower thermal efficiency.

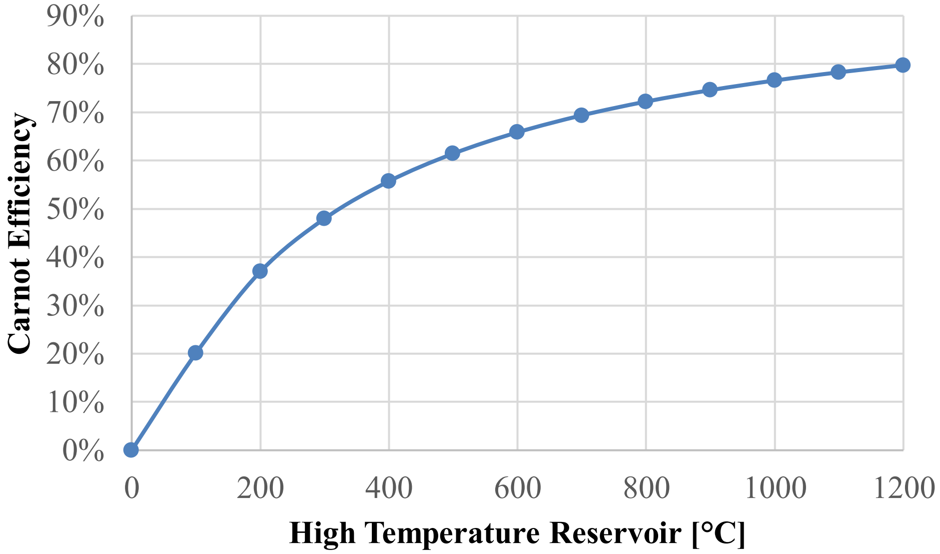

Figure 2.1: Carnot Efficiency as a Function of Heat Source Temperature (T_H), T_0=25 °C

2.2 Kalina Cycle

The Kalina cycle is a thermodynamic cycle invented by Alexander Kalina [9] that can be considered as a modification of the Rankine cycle. The major difference of this cycle from the Rankine cycle is the use of a mixture of two different fluids with different boiling points, most commonly ammonia-water, as a working fluid [10]. The process flow of a simple Kalina cycle is presented in Figure 2.2. This cycle consists of an expander, separator, absorber, pump, throttling valve, regenerator, condenser and evaporator.

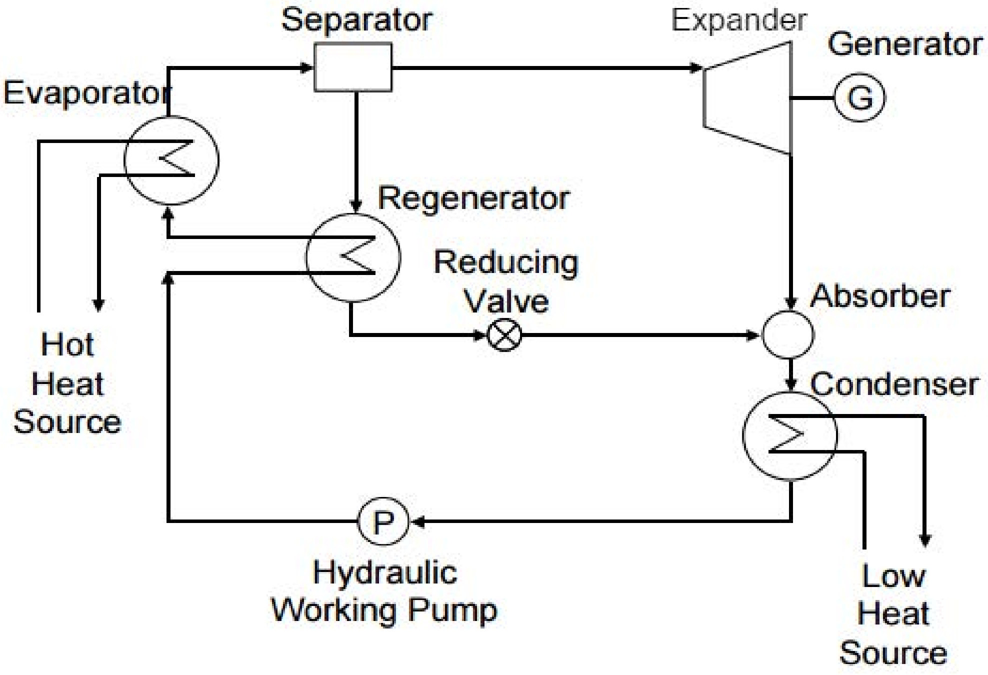

Figure 2.2: Component Diagram of a Simplified Kalina Cycle [10]

The working fluid mixture, ammonia-water, passes through the evaporator where it is heated by the hot source and partially evaporates, and then it is sent to the separator to separate the mixed liquid and vapor phases of the fluid. The separated liquid phase of the fluid is sent to the regenerator to be cooled, and then linked to the absorber after passing through the pressure reducing valve (throttling valve). The separated ammonia-rich vapor is sent to the expander where it drives the expander and produces the mechanical work that is, later on, optionally converted into electricity by means of a generator. The vapor stream leaves the expander as depressurized and cooled fluid and goes into the absorber where the two streams are accumulated and sent to the condenser. The fluid is, in this step, cooled by a low heat source and condensed to a complete liquid phase. Afterwards, the pump pressurizes the condensed liquid and sends the stream to the regenerator where the fluid is preheated by the separated liquid in the separator. The preheated fluid is, then, sent to the evaporator where it completes one cycle.

The main goal of this cycle is to, theoretically, increase the average heat absorption temperature corresponding to the value of T_H in the Carnot efficiency (see section 2.1) and decrease the average heat rejection temperature (T_L) by using azeotropic fluids. The feature of the azeotropic fluids that provides an advantage to the Kalina cycle over the Rankine cycle is that the temperature of the fluid does not stay constant even during the phase changes (non-isothermal process). As shown in Figure 2.3, the temperature increases during evaporation and decreases during condensation achieving the main goal mentioned above.

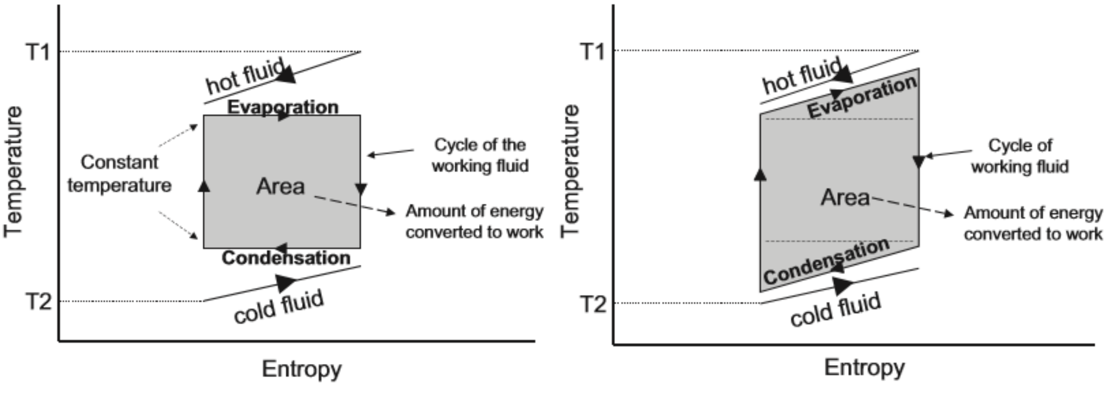

Figure 2.3: Comparison of Isentropic T-S Diagrams of Rankine (Left) and Kalina Cycle (Right) [10]

The Kalina cycle has been found to have higher performance potential in the heat recovery applications compared to the usual steam power plants as mentioned by Marston [11] and Corman et. al. [12]. Hettiarachchi et al. modeled and compared Kalina cycles to ORCs by using different mixtures of ammonia and water. They obtained higher thermal efficiencies with the Kalina cycle than the ORC for a given heat supply [13]. Park and Sontag also performed the second law analysis for the Kalina cycle and steam power cycle and they stated that the exergy efficiency of the Kalina cycle was 15% higher than that of the steam power cycle [14].

2.3 Transcritical CO_2 Cycle

The distinguishing feature of this cycle is that CO_2 is used as a working fluid. CO_2 being a natural refrigerant is a non-flammable, non-toxic, and inexpensive fluid that is abundant in nature [15]. In addition to that, it also has the advantage of better temperature profile matching between the heat source and working fluid (no pinch limitation) compared to the other fluids, as shown in Figure 2.4. This fact allows less irreversibility during the cyclic operation [16].

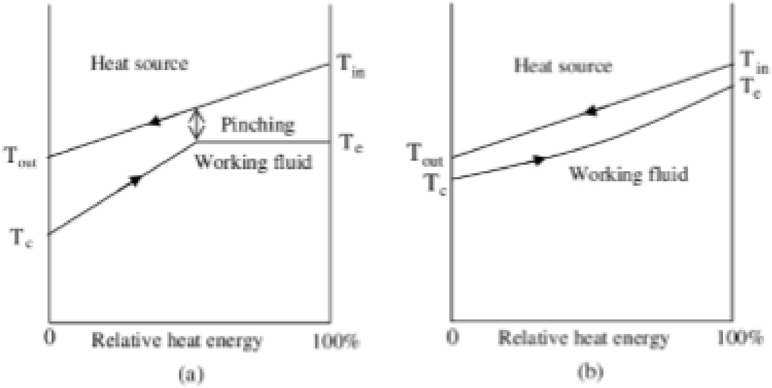

Figure 2.4: R123 (left) vs CO_2 (right) Heat Transfer [16]

CO_2's relatively low critical temperature (31.10 °C [17]) allows the cycle to operate close to the triple point, which decreases the amount of work needed to compress the fluid. The main drawback of this cycle is the fact that the high working pressure of this cycle must be higher than 73.8 bar in order to achieve supercritical conditions [15]. Therefore, the capital cost of the system will be higher compared to the subcritical cycles due to the requirement of thicker piping and pressure vessels [18].

Kinnaly and Nuszkowski emphasize using an expander to recover pressure drop in a throttling process of the CO_2 cycle, which, they believe, can increase the efficiency of the cycle up to 35% [17,19]. The transcritical cycle could then be competitive with traditional cycles. Chen et al. conducted a comparative study between a traditional ORC using R123 as a working fluid and a transcritical CO_2 cycle with a 150 °C heat source [20]. From the simulation results, they found that the transcritical CO_2 cycle had slightly higher efficiency over the ORC; confirming that the theoretical efficiency of the CO_2 cycle should have a higher performance than an ORC [20,21].

2.4 Stirling Engine

The Stirling engine is a regenerative cycle invented by Robert Stirling in 1816 (patent no. 4081) [22]. A simple Stirling cycle consists of a cylinder that includes two pistons in each chamber and a regenerator in the middle, and it comprises four thermodynamic processes. The main difference between this cycle and the Carnot cycle is that the Stirling cycle involves two constant-volume regeneration processes, whereas two isentropic processes take place in the Carnot cycle. The T-s and P-v diagrams of the Stirling cycle are shown in Figure 2.5 (a) and (b).

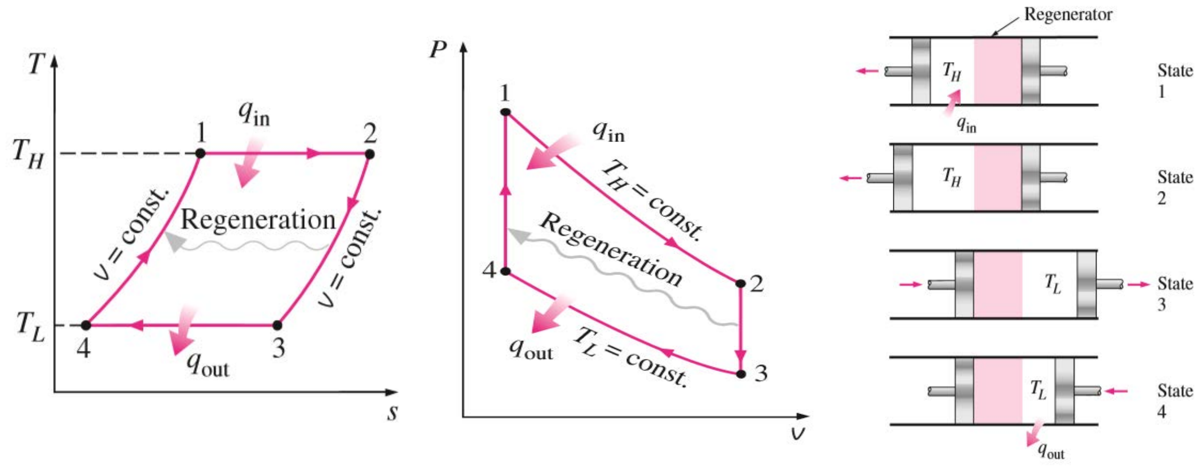

(a) (b) (c)

Figure 2.5: (a) T-s and (b) P-v Diagrams and (c) Demonstration of an Ideal Stirling Cycle [23]

The thermodynamic processes shown in the diagrams above are:

- Isothermal expansion 1-2: heat is added externally to the first chamber at the high temperature, T_H. The piston in the first chamber moves outward isothermally, thereby increasing the volume and decreasing the pressure.
- Constant-volume (isochoric) regeneration (heat removal) 2-3: both pistons move at the same rate to keep the total volume constant. The fluid moves into the second chamber while the heat is absorbed by the regenerator in the middle of two chambers. The temperature of the fluid is, therefore, reduced to T_L.
- Isothermal compression 3-4: the piston in the second chamber moves inward, thereby decreasing the volume and increasing the pressure. In the interim, heat is transferred from the fluid to the heat rejection sink at T_L to keep the temperature of the fluid constant at T_L.
- Constant-volume (isochoric) regeneration (heat addition) 4-1: both pistons move at the same rate to keep the total volume constant. The fluid in the second chamber moves

into the first chamber while the heat stored by the regenerator is transferred back to the fluid. This increases the temperature of the fluid to T_H and completes one cycle.

The heat addition to the Stirling cycle, demonstrated in Figure 2.5, occurs externally, which provides an advantage to use any kind of heat source to run the cycle. However, the external heating also decreases the amount of heat transferred into the system as mentioned by Tarique [24]. For this cycle, it is recommended to use a working fluid that has high thermal conductivity, low viscosity, low density and good specific heat capacity. The working fluids that are most commonly used and give relatively higher performance are helium and hydrogen [15,16,22,23,24,25,26]. The Stirling engines can be applicable to low temperature heat recovery systems such as waste energy, solar power, geothermal sources, etc. [22,25,26].

2.5 Thermoelectric Generators

The thermoelectric generators (TEGs), also called the Seebeck generators, are not power cycles but devices that generate a voltage differential from a heat flux. TEGs work on the principle of the Seebeck effect that was discovered by Thomas Seebeck in 1821. When a temperature gradient is applied to a semiconductor, the heat flowing between the hot and cold ends will generate an electromotive force (EMF) due to the charge carrier diffusion and phonon drag [27]. The voltage differential generated via these devices is defined by:

$$\Delta V = \alpha \Delta T$$

where ΔV is the voltage differential, ΔT is the temperature gradient and α is the Seebeck coefficient. The Seebeck coefficient is a property of the conductor and limits the performance of these devices. A simple TEG is composed of several semiconductors connected in series in order to achieve a usable high voltage as shown in Figure 2.6. The electrons in N-type semiconductors move freely from the cold to the hot side, whereas they move oppositely from the hot to the cold side, in the same direction of the heat, in the P-type semiconductors.

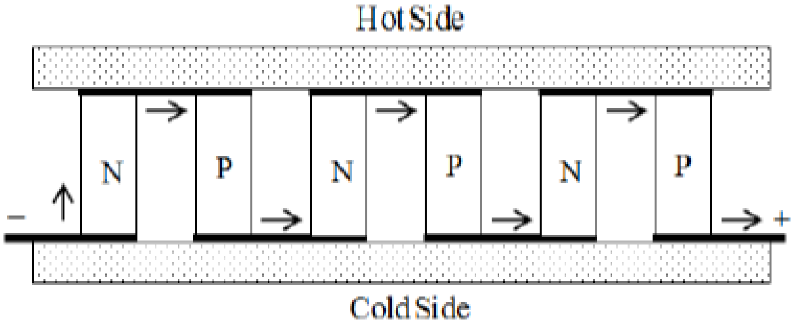

Figure 2.6: The Arrangement of the P and N-type Semiconductors in a TEG [28]

Different arrangements and configurations of the semiconductors can be made to achieve higher efficiencies using particular materials. The advantage of these devices is that the TEGs can directly convert heat into electricity without any need for moving parts. However, the efficiencies of TEGs are quite low. Kumar et al. performed a numerical modeling and analysis of a TEG for automotive waste heat recovery systems [29]. They obtained a power output of 552 W that corresponded to an electrical efficiency of 3.3%. They also stated that TEGs could meet the electricity need of medium-sized vehicles by utilizing the exhaust waste heat.

2.6 Organic Rankine Cycle

The Rankine cycle is a well-developed traditional thermodynamic cycle with a long history. It is the most commonly used cycle in power generation and considered as the model for the simple steam power plant [3]. This closed vapor power cycle is composed of four components, which are an expander, pump, evaporator and condenser. The working fluid is pressurized via the pump and it is sent to the evaporator where it reaches the saturated or superheated vapor point. Then, it passes through the expander, generates the shaft work and is condensed into the liquid phase by a cooling source before returning to the pump.

The usual working fluid used in Rankine cycles is water. In the case of utilizing a low temperature source, water is not the recommended fluid due to its high boiling temperature and pressure, and its low efficiency under low temperature heat source conditions. The Organic Rankine Cycle, also called low-temperature Rankine cycle, differs from the Rankine cycle in using organic fluids as the working fluid. Organic working fluids provide an increase in cycle performance compared to water-steam at low power levels but, this advantage disappears at 300 kW or more due to their poor heat transfer properties [15].

The ORC is the most widely used cycle to produce electricity from low temperature heat sources [30,31]. These sources can be based on waste heat [32,33,34], solar power [35,36,37], geothermal power [38,39], and biomass power [35]. The organic working fluids have low boiling thermodynamic properties that provide an advantage to the ORCs over traditional cycles. They are more economical and effective in sources as low as 80 °C [38-40].

2.6.1 Cycle Configurations

The ORC produces power by taking advantage of the amount of energy that can be extracted from the working fluid in the saturated or superheated vapor phase while requiring only a small amount of work to pressurize the working fluid. The configuration of the basic ORC, the model for traditional low-grade heat source power cycles, is shown in Figure 2.7. The advantage of the organic fluid, used in ORCs, allows low grade heat sources to be utilized with higher performance. Engin and Ari [41] conducted an energy audit analysis of a kiln system working in a cement production plant in Turkey. They found that approximately 40% of the total input energy was lost as a waste energy through the hot flue gases, cooling stack and kiln shell. This waste energy was at temperatures between 215 °C and 315 °C.

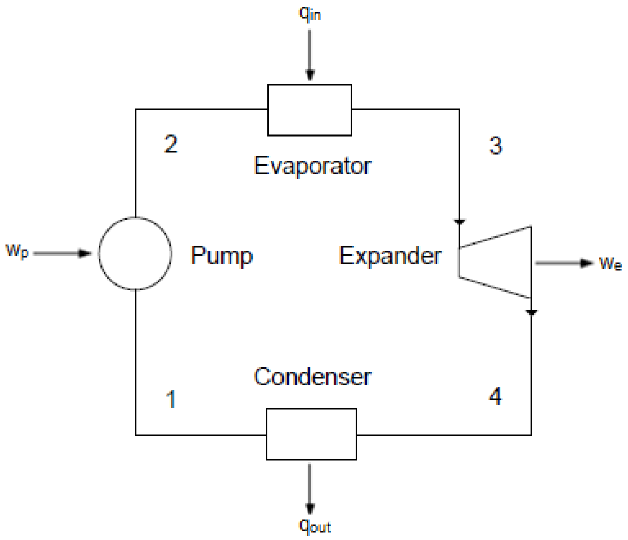

Figure 2.7: Component Diagram of a Basic Organic Rankine Cycle [28]

The basic Rankine cycle shown above can be reconfigured with the inclusion of additional heat exchangers, pumps, and condensers in order to achieve higher efficiency. However, these component additions will increase the cost and they can also hurt the overall power plant efficiency if the system is not optimized [42]. Saleh et al. [42] conducted thermodynamic property analysis of 31 different working fluids (alkanes, ethers, fluorinated alkanes and fluorinated ethers) in different ORC configurations. They obtained the highest thermal efficiency in subcritical configurations with a regenerator. They also stated that the shape of the saturated vapor line of the fluid and the state of the vapor entering the expander should be evaluated carefully when considering the configuration of the cycle. Another common configuration of the ORCs is the regenerative ORC as presented in Figure 2.8.

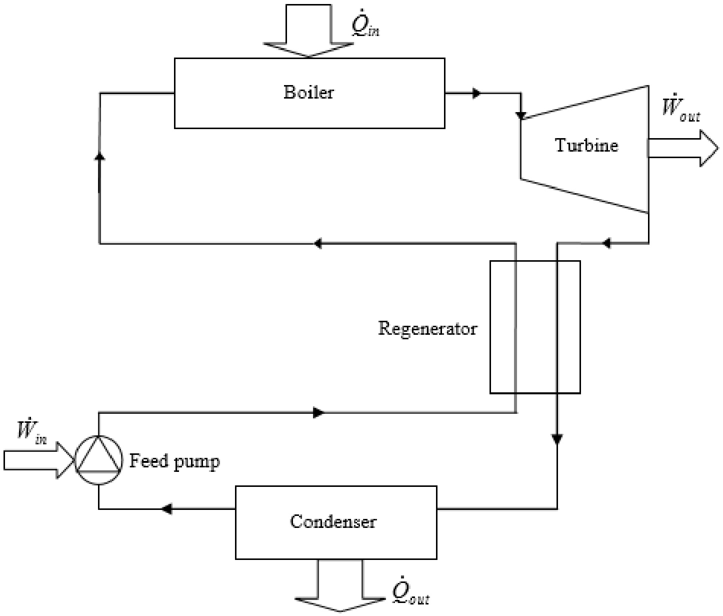

Figure 2.8: Regenerative Configuration of ORC [24]

2.6.2 Working Fluids

The selection of the organic fluid has a profound impact on the thermal efficiencies of ORCs. The classification of organic working fluids can be divided into three main categories by their saturated vapor lines in a T-s diagram as shown in Figure 2.9. The slope of these saturated vapor lines can be negative (dT/ds<0), positive (dT/ds>0), or infinitely large (dT/ds=0) for wet fluids, dry fluids and isentropic fluids, respectively [43].

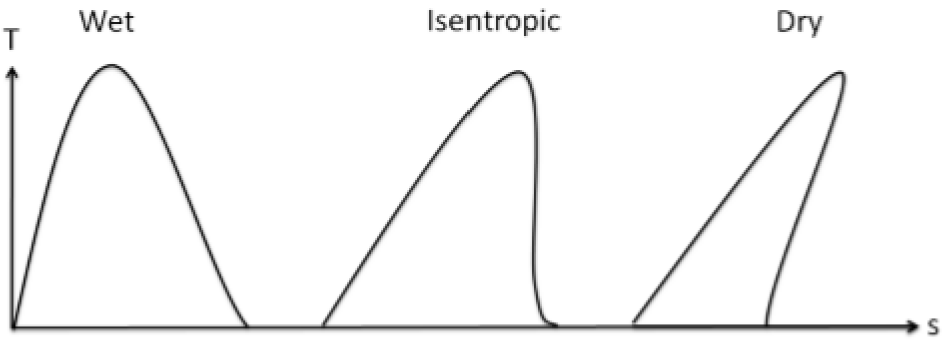

Figure 2.9: T-s Diagrams of Different Type of Organic Working Fluids [15]

Quoilin et al. [44] suggest reviewing the following criteria for fluid selection:

- Thermodynamic properties: for given temperature reservoirs, the performance of the cycle depends on the expander-fluid, the reservoirs fluid-temperatures, and the compatibility of the expander-temperatures. Therefore, the thermodynamic properties of the fluid such as critical points, acentric factor, density, specific heat, etc. should be considered carefully.
- Positive or isentropic saturation vapor curve: due to the two-phase mixture interaction of wet fluids with the expansion machine, dry or isentropic fluids are considered as the most well suited working fluids for ORC. However, the phenomenon of wet fluids can be overcome by using positive displacement machines, which are compatible with operating in two-phase conditions.
- High vapor density: low vapor density will result in a larger volumetric flow rate, which will lead to an increase in pressure drop within the heat exchangers and a requirement of a larger expander. Consequently, this will increase the size and the cost of the system.
- Low viscosity: low viscosity is needed to maintain a high heat transfer rate and to decrease the frictional losses.

- High thermal conductivity: important to have a high rate of heat transfer in the heat exchangers.
- Optimal evaporating pressure and positive condensing pressure: a fluid with higher evaporating pressures requires higher costs and more complicated configurations. To prevent air infiltration in the system, the condensing pressure should be higher than the atmospheric pressure.
- Safety and environmental considerations: flammability, toxicity and environmental effects of the fluid such as ozone depleting potential (ODP) and greenhouse warming potential (GWP) should be taken into consideration.
- The melting point: this value should below the lowest ambient temperature to prevent freezing of the fluid.
- Availability and cost: lower cost fluids that are easy to acquire should be preferred.

Tchanche et al. [45] conducted a thermodynamic characteristic and performance analysis of different working fluids by considering several criteria. They concluded that only a number of the working fluids are suitable for low temperature ORC with heat sources below 90 °C. The important parameters of these fluids are presented in Table 2.1.

Table 2.1: Working Fluids for Low Grade Heat Sources [45]

Fluid	Type	Molecular Mass (kg/kmol)	T_{crit} (°C)	P_{crit} (MPa)	Boiling Temp.	GWP	ODP	ASHRAE 34
R134a	Isentropic	102.03	101	4.059	-26.1	1430	0	A1
R152a	Wet	66.05	113.3	4.52	-24	124	0	A2
R600	Dry	58.12	152	3.796	-0.5	20	0	A3
R600a	Dry	58.12	135	3.647	-11.7	20	0	A3
R290	Wet	44.1	96.68	4.247	-42.1	20	0	A3

2.6.3 Irreversibilities

As is the case with all processes, the ORC has inherent losses due to different types of irreversibilities. These factors can occur in the form of heat losses, leakages, friction losses, pressure drops in valves and pipes. Hung [46] conducted a parametric irreversibility analysis of the ORCs and he stated that, theoretically, the irreversibility affecting the overall efficiency occurs in the heat transfer processes in the evaporator and the condenser due to the highest enthalpy changes occurring in these components. He also showed that the irreversibility tends to decrease as the inlet pressure of the turbine increases at constant turbine inlet temperatures as shown in Figure 2.10.

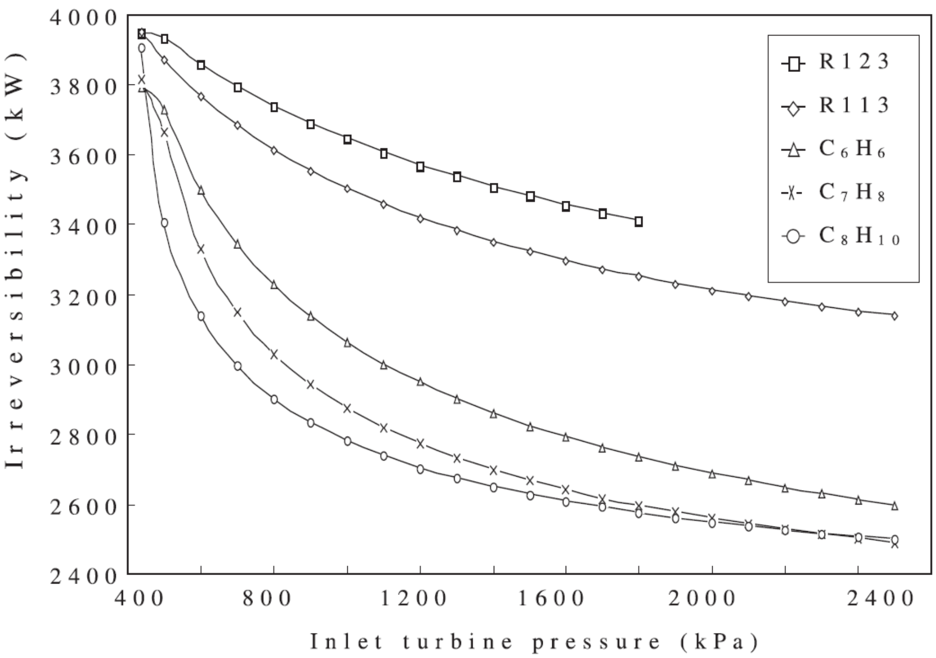

Figure 2.10: Irreversibility-Turbine Inlet Pressure Relation for Different Working Fluids at Constant Inlet Temperature [46]

The largest portion of irreversibility in a cycle that occurs in evaporation and condensation processes as mentioned are caused by the temperature profile differences between the working fluid and the heat sources. Larjola [34] emphasizes that for moderate temperature heat recovery systems, organic working fluids show higher performance and power output compared to water-steam Rankine cycle due to the small amount of energy needed for vaporization and better temperature profile matching with low grade heat sources.

2.6.4 Cycle Improvements

There are certain ways to improve the performance of a cycle. However, most of the variations cannot be easily implemented to a cycle after the configuration is complete. The highest efficiency a thermodynamic cycle can achieve is limited by the temperatures of the reservoirs as aforementioned. These temperature values define the maximum heat transfer that can occur in a particular system.

Increasing the heat source temperature or decreasing the rejection sink temperature would increase the overall efficiency. However, it is usually not possible to modify the temperature of the heat rejection sink and the heat source when it comes to low temperature energy recovery. Therefore, in order to enhance the overall performance of ORCs the attention should be focused on the compatibility between the working fluid and the expander, the addition of a regenerator, and mechanical and thermal efficiencies of the components. The heat transfer efficiency in the evaporator and the expander efficiency are considered as the main factors for efficiencies of low temperature energy recovery systems.

2.6.5 Applications

There is no standardized classification of heat sources based on their temperature range but, different classifications are taken into considerations by many studies in the literature. As aforementioned, Imran et. al [7] consider temperatures below than 230 °C as low temperature heat sources. Peterson et. al [47] consider low-grade heat sources for temperature below than 150 °C, moderate-grade for a range of 150-400 °C and high-temperature for temperatures higher than 400 °C. Saleh et. al [42] mentioned that the low temperature was approximately 100 °C and medium temperature was approximately 350 °C. According to U.S. Department of Energy [48], the heat sources are categorized as low-quality for a temperature range of 0-232 °C, medium-quality for a range of 232-650 °C and high-quality for temperatures above 650 °C.

The heat sources most commonly used in ORC applications can be divided into three main categories as stated by Quoilin [16]:

- Waste heat: As mentioned by Larjola [34], the ORCs are considered as the most useful cycles for waste heat recovery systems since they can use organic fluids which provide the best performance and the highest power output in low-grade energy recovery compared to the traditional cycles. Hung et al. [33] indicated that 50% or more of the overall heat generated in industry has been released to the atmosphere in the form of low-grade energy, which also causes environmental concerns due to thermal pollution. Waste heat recovery using ORC can also be applied to the Combined Heat and Power (CHP) plants, cement production plants, biomass plants, exhaust gasses of vehicles, and the condenser of power cycles.
- Solar power: solar power is another heat source that can be used in ORCs since the temperatures reached by solar panels are relatively low. Manolakos et al. [49] conducted an experimental study on the performance analysis of a low-temperature solar ORC (SORC) using HFC-134a as the working fluid for reverse osmosis (RO) desalination. They obtained a maximum overall system efficiency of 4% and approximately 2.05 kW of maximum power generation, which they believe is sufficient to drive the RO unit.
- Geothermal plants: the temperature of geothermal heat sources vary from 50 to 350 °C and the source can be steam, mixture of steam and liquid, or only liquid water. Hettiarachchi [38] et al. considered geothermal sources as low-temperature for a range of 70-100 °C and they showed that the ORC efficiency using a geothermal heat source is highly dependent on the working fluid selection and the geothermal water temperature.

2.7 Comparison of Low Temperature Energy Recovery Methods

The methods mentioned above have their own advantages and disadvantages over each other depending on a variety of working conditions such as pressure, temperature, working fluid, etc. The transcritical CO_2 and Kalina cycles are, theoretically, promising thermodynamic cycles with high performance. However, they have not been widely proven in the literature and, therefore, are not common in a wide range of applications. Due to their high operating pressure conditions, these two cycles also require thicker materials which may significantly increase the capital costs of the systems. The high toxicity of ammonia limits the material selection in the Kalina cycle. The Stirling engine and TEG also promise high thermodynamic performance. The main drawback of the Stirling engine is the required operation at very high temperatures and pressures. The ORC has a minimal number of components and is a well-developed technology with a long history of research. It allows the use of a number of working fluids which can operate well with a variety of heat sources. The ORC can also have high performance under a wide range of temperature and pressure working conditions.

2.8 Expansion Machines

The expander is a key part of the ORC that has an impact on the overall performance and efficiency of the system. There are many types of expansion machines, each of which can work well under different system parameters and working fluids. The selection of the most suitable expander plays a key role in achieving the optimum thermal efficiency.

Expansion machines, in general, can be divided into two main categories by their designs and working principles. These categories are dynamic machines, such as turbomachinery, and positive displacement machines, also called volumetric expanders [15]. Positive displacement expanders include scroll, screw, rotary vane, gerotor, reciprocating piston, rotary (rolling) piston and free-piston linear expanders. The parameters that should be considered when selecting an expander are high isentropic efficiency, pressure ratio, power output, rotational speed, dynamic balance, complexity, lubrication requirements, reliability, and cost as indicated by Harada [15].

2.8.1 Turbomachinery

Turbines are dynamic rotary expansion machines and can be classified into two main categories, which are axial turbines and radial turbines [50]. In axial turbines, fluid enters and exits the turbine in parallel with the axial direction of the rotor and based on their blade shapes, these turbines are classified as impulse and reaction turbines. Figure 2.11 illustrates three types of turbines.

Reaction turbines take advantage of lift force. In impulsive turbines, the high pressure fluid is passed through a nozzle, increasing its velocity, and is directed into a set of bucket-shaped or scoop-shaped blades [18]. The kinetic energy of the accelerated fluid is absorbed by the blades, leading to the motion of the rotor.

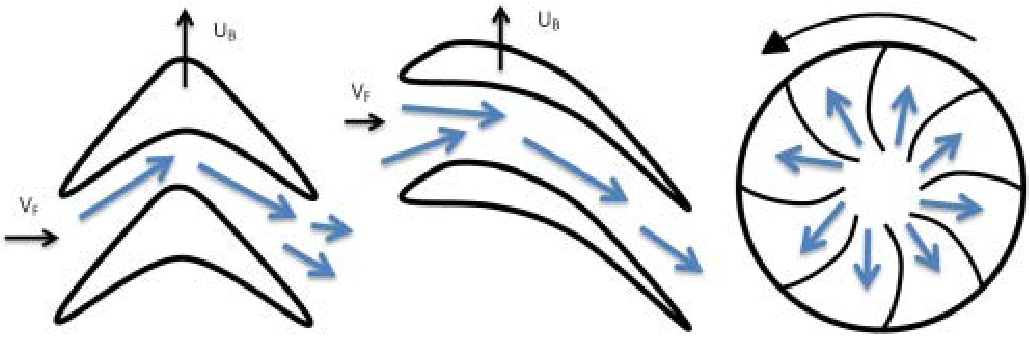

Figure 2.11: Turbine Types: Impulse Turbine (left), Reaction Turbine (Middle), and Radial Inflow Turbine (right) [15]

In radial inflow turbines, the fluid enters the turbine in the axial alignment of the center of the turbine shaft and leaves at 90° angle to the turbine shaft. Based on the direction of flow, there are two different configurations of these turbines, centripetal (towards the center) and centrifugal (away from the center), as shown in Figure 2.12.

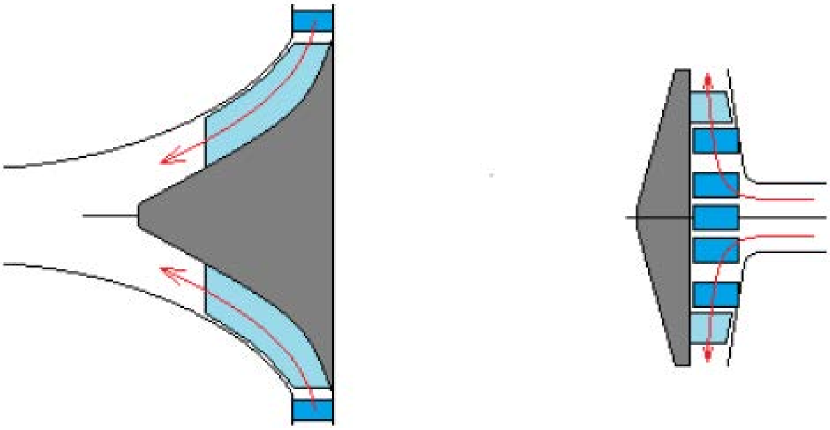

Figure 2.12: Centripetal (left) and Centrifugal (right) Turbines [50]

To evaluate the performance of turbomachinery, there are several parameters that need to be compatible with each other. However, one of the parameters that plays a key role in the efficiency of turbomachinery is the tip speed, v, of the machine. Pressure ratio, which is the ratio of the pressure drop per stage, determines the number of stages of the turbomachinery and is also dependent on the tip speed [18]. There are two major tip speed-dependent losses in displacement machines, the leakage and throttling losses. As the tip speed increases, the leakage losses are reduced, but the throttling losses will increase [51]. The term of optimum tip speed is then defined and can be determined for any turbomachinery. The optimum tip speed is fairly independent from the machine size, as indicated by Persson and Sohlenius [51], and is related to the shaft speed, n, with the following fundamental relation:

$$n = (v * 60)/(\pi * D)$$

where D is the diameter of the expander. From this relation, it can be shown that the expander will have to rotate at much higher rotational speeds as the diameter decreases in order to operate at the optimum tip speed and maintain good performance. This fact makes it impractical to use a small turbine in applications.

Depending on the design and operating conditions of the turbomachinery, the primary source of loss can differ. Due to the interaction of the fluid with the surfaces of the blades, the housings, and the rotor hub, fluid friction occurs in the boundary layer. The boundary-layer losses can be considered as the inevitable and most important loss source of up to 30 percent of the machine output [18]. Another source of loss is due to the blade tip leakage. A portion of the fluid flow tends to leak from the clearance between the blade tips and the housings resulting in a loss due to the decrease in the mass flow and the change in the flow pattern in the blade tips. This clearance is machine-sized and kept to a minimum regardless of the size of blades. For large blades, the tip leakage losses amount to 1-2 percent. However, relatively the same loss may account for 10-15 percent in small scale turbines [18]. Other sources that contribute to loss in efficiency include seal leakage (1%), eddy losses (1-2%), moisture churning (1% per 1% of moisture), and bearing losses (<1%) [18].

Yamamoto et al. [52] performed a numerical and experimental study on the efficiency of an ORC using a micro-turbine. The turbine was a radial type, made of aluminum, with 18 blades, 30 mm in diameter and 4.5 mm thick. The maximum isentropic efficiency that the turbine achieved was shown as 46%, however, any deviation from the designed conditions caused a rapid decrease in the turbine efficiency. The maximum cycle efficiency was obtained as 1.25% by using HCFC-123 as the working fluid.

Yagoup et al. [53] conducted an experimental study on a micro-CHP ORC utilizing solar energy as the heat source. The total capacity of the solar source was 25 kW and the maximum turbine capacity was 1.5 kW. The turbine rotated at 60,000 RPM and they achieved 85% turbine isentropic efficiency using HFE-301. The maximum electrical and overall cycle efficiencies were obtained as 7.6% and 17%, respectively.

Kang [54] designed a radial turbine with a pressure ratio of 4.1 and an ORC. He also conducted experiments in different evaporator temperatures to analyze the efficiencies and the operational characteristics of the system. He showed that the efficiencies of both the turbine and overall cycle increased as the evaporator temperature increased. Maximum average cycle and turbine efficiencies and power output were achieved as 5.2%, 78.7%, and 32.7 kW, respectively, using a low temperature heat source and R245fa as the working fluid.

2.8.2 Scroll Expander

The scroll expander is a volumetric expander that consists of two identical scroll wraps fixed to their back-plates. These two scroll wraps are nested inside each other where one is fixed to the compressor and the other is attached to the crank shaft and allowed to rotate in its orbit. The working principle of the scroll expanders are based on the interaction of these two scroll wraps. The high pressure-temperature working fluid enters the expander from the suction port in the center of the expander. The motion of the rotating scroll in its orbit creates an increase in the volumes of the chambers where the working fluid is trapped. The step-by-step increase in the volumes of the chambers causes the fluid to expand until the fluid reaches the discharge ports at the outer edges of the scroll wraps. The low pressure-temperature fluid is then exhausted. This process is illustrated in Figure 2.13.

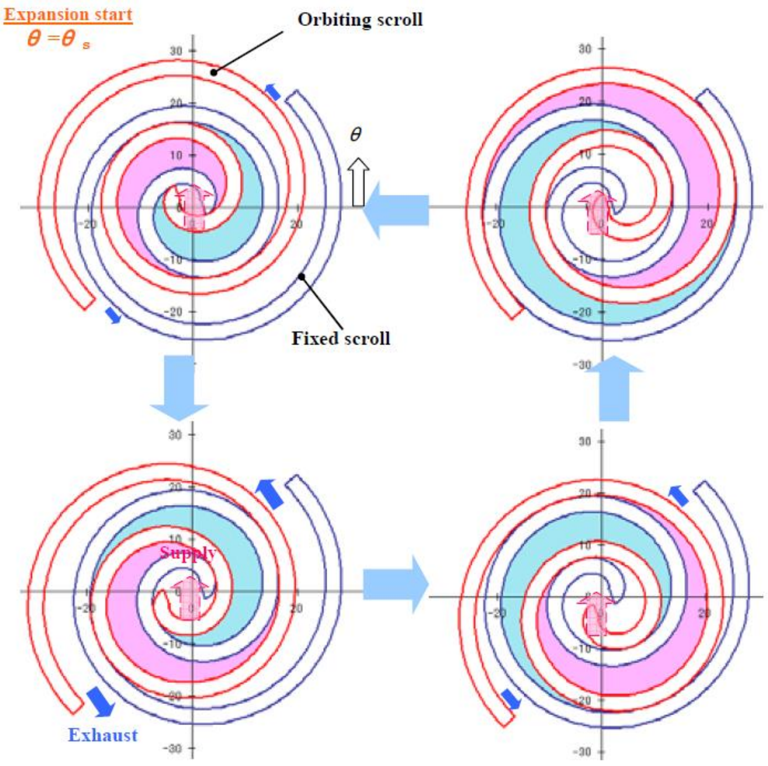

Figure 2.13: Working Process of a Scroll Expander [55]

There are two types of scroll expanders; compliant type and kinematically constrained type. The constrained type of expanders is usually made of three cranks separated from each other by an angle of 120°. The orbiting scroll is constrained axially, radially, or both. Thus, two scroll wraps do not interact with each other during the operation and there is a small clearance gap between them. Therefore, they do not require lubrication, but sealing becomes the paramount factor on their performance. The gaps have to be minimized during manufacturing to reduce leakage losses. Constrained expanders are more effective when used at higher rotation speed because the time that the working fluid has to escape from the chambers is reduced at higher speeds. In the compliant type of expanders, however, an orbiting scroll is present and they use the centrifugal effect during operation. The scrolls are always in contact. Therefore, lubrication is needed to prevent overheating of the scrolls and to reduce frictional losses. Low friction materials are used in the compliant scroll types for sealing and they have better sealing compared to the constrained types [15]. In scroll expanders, there are two leakage passages; radial leakage and flank leakage, as illustrated in Figure 2.14 [56].

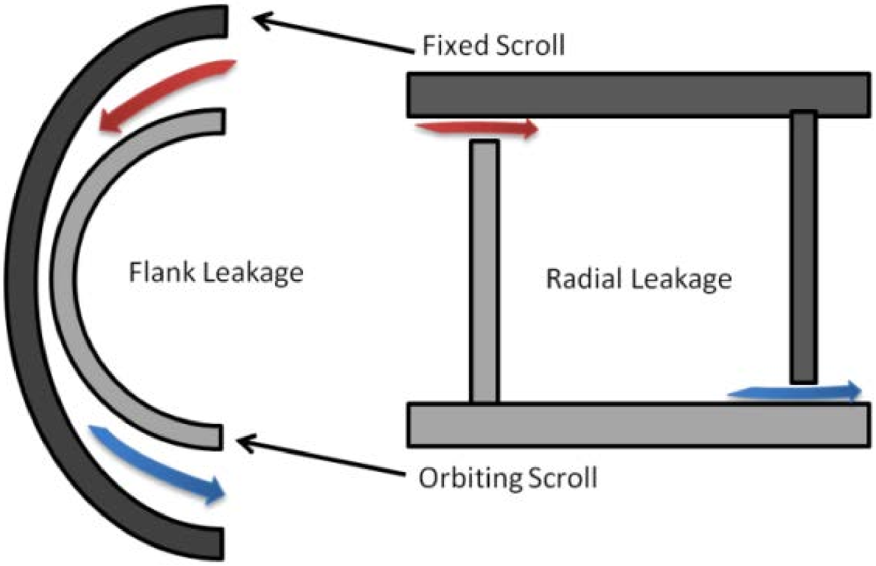

Figure 2.14: Flank and Radial Leakages [56]

Scroll expanders are commonly used in small power output applications with a wide range of isentropic efficiencies between 50-89% as indicated by Kinnaly and Nuszkowski [17]. An experimental study by Lemort et al. [57] was carried out on a prototype of an open-drive oil-free scroll expander using HCFC-123 in an ORC. The results showed that the tested prototype reached a maximum isentropic efficiency of 68%. Another experimental study by Mathias et al. [58] was conducted on a scroll expander used in an ORC. They obtained an isentropic efficiency of 83% for the scroll expander with an electric production of 2.96 kW. They also concluded that the scroll expanders were good candidates to be used in power production from low-grade energy.

2.8.3 Screw Expander

The screw expander, a type of volumetric expander, was developed to utilize the energy in geothermally hot water in the 1970s [59]. They can have expansion ratios up to 3:1 [50]. Two different screw expander designs exist: the twin screw and single screw designs.

The twin screw expander consists of three parts; a casing and a meshing pair of two helical screw rotors that are called female and male rotors. The male rotor is known as the rotor with a larger diameter, whereas the female rotor has smaller thickness. Helical screws of both rotors mesh and rotate in opposite directions. The fluid flows through the intake port. As the pressurized hot fluid drives the rotors (mechanical energy extraction), the volumes of v-shaped expansion chambers increase, thereby leading to the expansion of the fluid. Then, the depressurized warmer fluid is exhausted when the expansion chamber reaches the discharge port. Figure 2.15 illustrates the operation of a twin screw expander from intake to discharge.

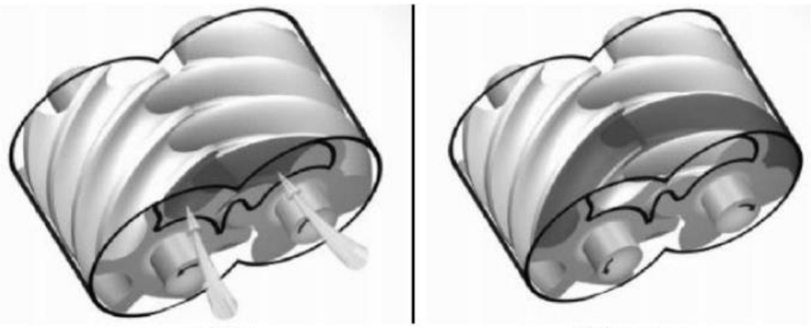
i.) Filling

ii.) Expansion

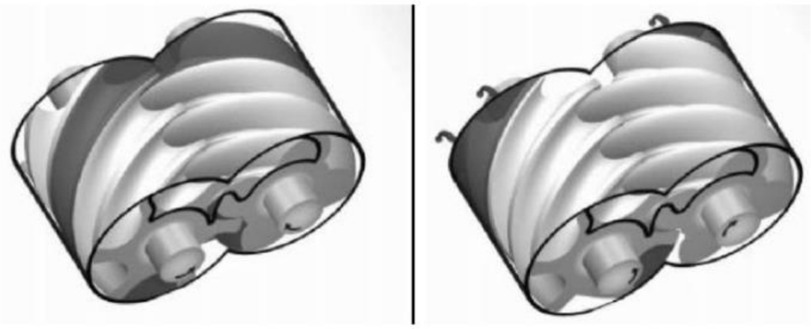
iii.) End of Expansion

iv.) Discharge

Figure 2.15: Working Processes of a Twin Screw Expander [17]

The single screw expander, on the other hand, has a single helical screw rotor (main rotor) with, additionally, two gate rotors located symmetrically on each side of the main rotor. The only difference in the working process of the single screw expander from the twin screw expander is that the fluid is trapped with the gate rotors instead of using two helical rotors. Figure 2.16 shows the working processes of a single screw expander.

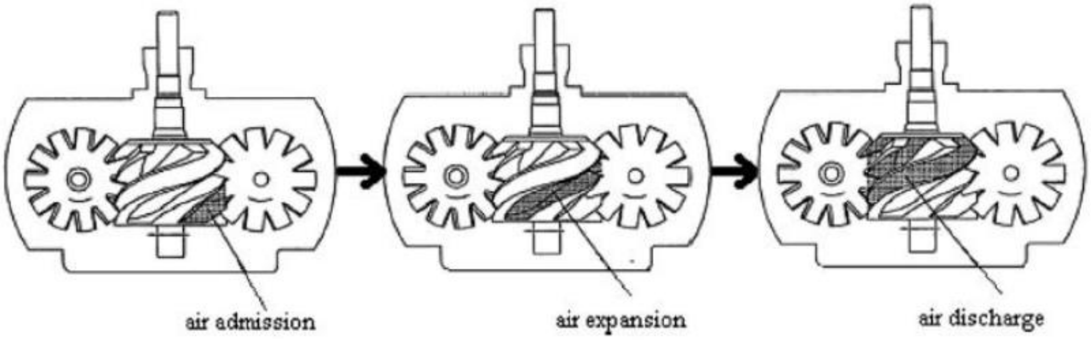

Figure 2.16: Working Mechanism of a Single Screw Expander [60]

For efficient operation of the screw expanders, Smith et al. [61] suggests the following:

- Maximum flow area between the lobes and casing
- Minimum leakage
- Optimum choice of built-in volume ratio
- Optimum choice of tip speed

The main challenge of the screw expanders is preventing the internal leakages between the expansion chambers and between the shafts and casing while keeping the contact surface friction minimized [50]. Two methods for screw expanders have been developed to overcome this situation: oil-free and oil injection designs. In oil injection designs, the working fluid is mixed with oil in order to seal the clearances, lubricate the rotor motion, and prevent overheating of the machine. No internal sealing is required in this type of design. It has a simpler mechanical design, is inexpensive to manufacture and highly efficient [62]. In the oil-free machines, oil is separated from the working fluid and lubrication of the bearings is done externally. Internal seals are required to avoid lubricant entering the rotor lobes. Timing gears are used to prevent contact between rotors. These additional parts require a more sophisticated design and manufacturing costs than needed for the oil injection design [62,63].

Screw expander applications include ORC, SORC, geothermal, refrigeration cycles, and trilateral flash cycle for low-grade heat sources [17]. Long term developments and investigations have been carried out by Smith et al. [61,62,64]. They emphasized that the screw expanders are the expanders most suitable with two-phase working conditions and they achieved a peak isentropic efficiency of 76% [62].

2.8.4 Rotary Vane Expander

Another type of volumetric expander is the rotary vane expander and it has a simple mechanical design consisting of a housing and rotor with sliding vanes. The design and operation of this expander are illustrated in Figure 2.17. Operation of this expander starts with the pressurized fluid entering the inlet (1). The sliding vanes that are located inside the rotor are pushed outward by the centrifugal effect driving the rotor and extracting the mechanical energy. As the vanes rotate, the volume in the expansion chamber increases (2-3). Thus, the fluid expands and, at the end, is discharged from the outlet (4).

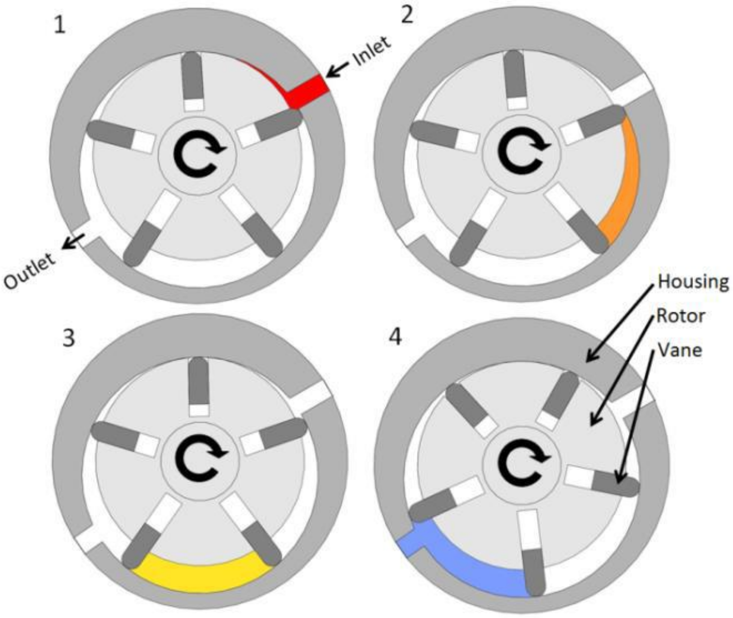

Figure 2.17: Design and Working Processes of a Rotary Vane Expander [15]

Rotary vane expanders have several advantages over other types such as low manufacturing cost due to their simple designs and minimal mechanical parts, capability of handling high pressure, high tolerances to operate under wet expansion conditions with little or no erosion [65,66]. They also have relatively high volumetric expansion ratios ranging up to 10 and cause low noise and vibration during operation [66]. Lubrication is required in order to enhance sealing, prevent overheating, reduce friction losses and minimize wear during operation [67]. It is also mentioned by Badr et al. [66] that the main power losses occur due to the pressure drop at the inlet accounting for 65% of the total loss, whereas leakage losses account for 20%.

In a study conducted by Yang et al. [68], a rotary vane expander prototype was tested in the transcritical CO_2 refrigeration cycle with a suction pressure range from 7.5 to 9.0 MPa and a suction temperature range from 32.4 to 44.3 °C. The optimal isentropic efficiency of 23% was obtained at 800 RPM. To clarify that the efficiency decreased at higher speeds, the authors concluded that the frictional losses increased more rapidly than the reduction in the leakage losses via better sealing at higher speeds. Kinnaly and Nuszkowski reported that the maximum output power output of a rotary vane expander in the literature was found to be less than 2 kW with an isentropic efficiency range between 23-73% [17].

2.8.5 Gerotor Expander

The gerotor is a volumetric rotary expansion machine that consists of an inner rotor and outer stator located eccentrically on the same shaft. In the design, the rotor has one less tooth than the stator and the expansion chamber volumes constantly change as the shaft is rotated by the high pressure fluid. The expansion process of the gerotor is shown in Figure 2.18. During half of each shaft rotation, the expansion chamber volumes increase (1-5) and they start decreasing through the second half of shaft rotation (6-10). Via inlet port, the fluid enters the expansion chamber at the minimum volume and expands as the volume increase. The depressurized fluid is forced out when it reaches the exit port. While the exhaust process occurs, the inlet port fills another chamber simultaneously as shown in Figure 2.18 by Frames 9-10 and 1-2 being in the same position.

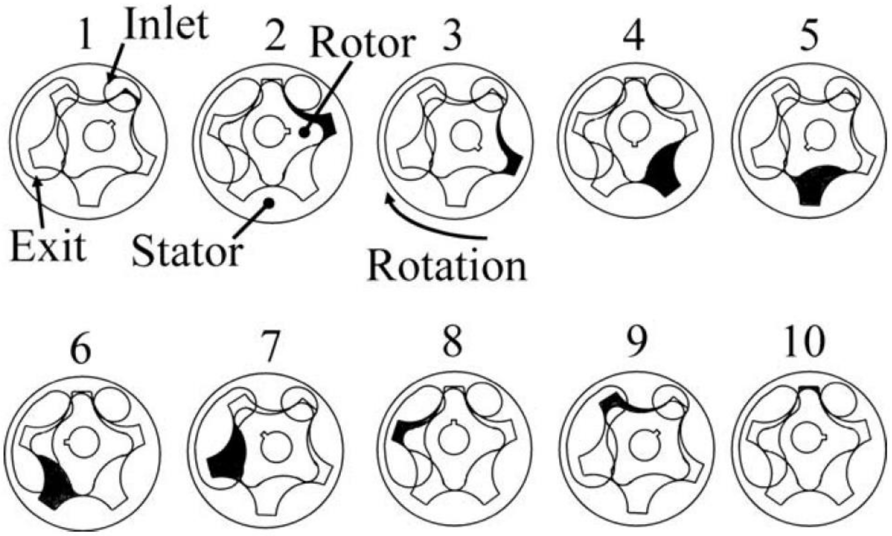

Figure 2.18: Working Processes of a Gerotor Expander [69]

A five-tooth stator (as in Figure 2.18) rotates at one-fifth shaft speed relative to the rotor. For instance, a shaft rotating at 3600 RPM will result in relative speed of 720 RPM between the rotor and stator. This fact gives an advantage of low friction to the gerotor expanders over the others. In addition, the sealing is assured with oil injection in the working fluid [69].

Mathias et al. [69] conducted an experimental study on gerotor expanders used in an ORC with the working fluid of R-123. They tested three different gerotors, which they identified as A, B and C, and showed the importance of the manufacturing tolerances. The gerotor A had an excessively large clearance between the rotors and the housing, and it did not produce power due to high leakage. Gerotor B had a very small clearance and it eventually failed due to the large amount of friction and excessive wear. Only the gerotor C showed good performance, producing 2 kW of power with an isentropic efficiency of

85%. Thus, they showed that the performance of the gerotor highly relied on the manufacturing tolerances.

2.8.6 Reciprocating Piston Expander

The reciprocating piston is another type of positive displacement machine that consists of a cylinder and a piston connected to a crankshaft. The cycle of this expander type experiences three different processes during operation: intake, expansion and exhaust. In the simplest design, the expander contains two valves, one of which is the intake valve and the other is the exhaust valve. The operation processes are illustrated in Figure 2.19.

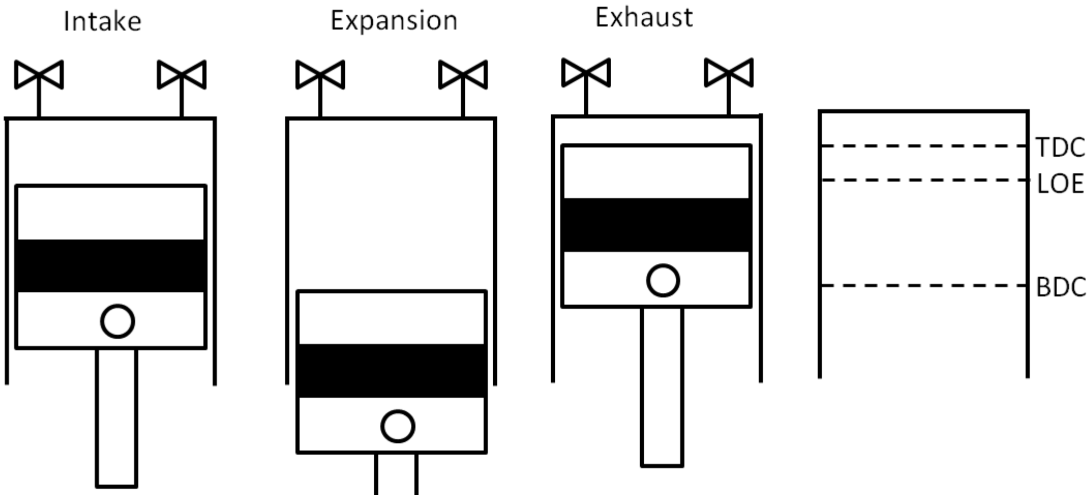

Figure 2.19: Operation of a Reciprocating Piston Expander [15]

The intake valve opens when the piston is at top dead center. The high temperature-pressure gas enters the cylinder, pushing the piston down. When the piston is at the location of expansion (LOE), the intake valve closes. The gas expands as the piston moves downwardly and the mechanical work is extracted by means of the crankshaft. When the piston reaches bottom dead center (BDC), the exhaust valve opens and the exhaust gas is expelled from the system by the piston moving upwardly. When the piston reaches TDC, the intake valve opens and, thus, one cycle is completed.

The reciprocating piston expander is very robust, which is an advantage over the other expanders. However, for efficient operation, they require structure balancing to prevent excessive vibrations and precise timing of the intake and exhaust valves with the piston motion [50]. Sealing is assured by the use of piston rings. The primary contribution to the performance losses is the friction due to the large contact surfaces between the rings and the cylinder wall. Therefore, a lubricant such as oil is also required to reduce the friction losses and to avoid excessive wear.

Zhang et al. [70] developed a double acting free piston expander to replace the throttling valve for work recovery in the transcritical CO_2 cycle. They achieved an isentropic expander efficiency of 62% and they also stated that utilizing a slider-based inlet/outlet control scheme led to proper operation of the expander and an increase in the efficiency. In another study by Baek et al. [71], a piston expander replaced the expansion valve in a transcritical CO_2 refrigeration cycle with a goal to increase the coefficient of performance (COP) of the system. The expander was a modified four-cycle, two-piston gasoline engine with a displacement volume of $2\times13.26\ cm^3$.The expander achieved an isentropic efficiency of approximately 11%, enhancing the system performance (COP) by up to 10.5%.

Glavatskaya et al. [72] modelled a semi-empirical reciprocating expander for exhaust heat recovery in an automobile application. The expander achieved a maximum isentropic efficiency of 70%. They also observed and stated that the isentropic efficiency of the expander increased with the rotary speed, but decreased as the pressure ratio on the expander increased.

2.8.7 Rotary Piston Expander

The rotary piston expanders are also positive displacement machines and they include several variations: single/two rolling piston, swing piston, and revolving vane. The difference between a swing piston and rolling piston expanders is that the swing piston expander does not roll, but swings instead. In the basic design, a rolling piston expander consists of a piston with a spring loaded sliding vane, a stator cylinder, and suction and discharge ports. The rolling piston is connected to a crankshaft eccentrically. Figure 2.20 illustrates the three processes of the operation. The high pressure-temperature working fluid enters the inlet (1) and starts the rolling of the piston. As the piston rolls, the mechanical work is extracted and the chamber volume increases, leading to the expansion of the fluid (2-3). At the end of the expansion, the fluid is exhausted via the discharge port (4).

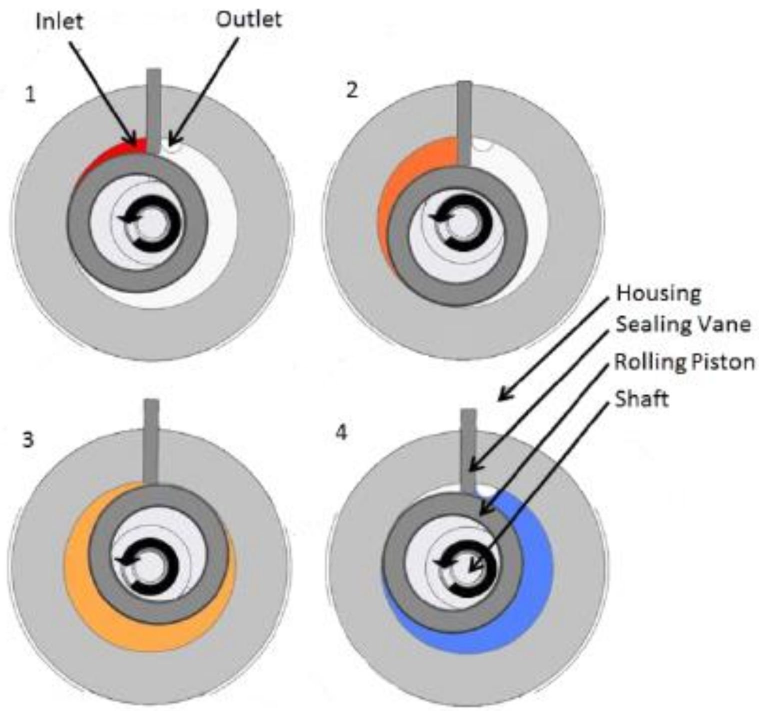

Figure 2.20: Intake, Expansion, and Discharge Processes of a Rolling Piston Expander [15]

These types of expanders are able to handle very high pressures, and also have simple designs with few parts. The main sources of performance losses are friction and internal leakages. Lubrication is necessary to minimize friction and wear, and to assure sealing. The primary internal leakage occurs at the interaction surfaces of the piston and the cylinder wall due to the high pressure differential between the neighboring volumes [73].

Wang et al. [74] conducted an experimental study on a rolling piston expander used in a solar Rankine cycle with R-245fa as the working fluid. The tested expander achieved an average isentropic efficiency of 45.2% at 800-900 RPM, producing an average power output of 1.73 kW. Haiqing et al. [73] developed a swing piston expander prototype to replace the throttling valve in a CO_2 transcritical cycle. They obtained an isentropic efficiency range generally between 28% and 44% for the expander and mentioned that the friction and leakage losses must be evaluated carefully in the design of this type of expander. Jiang et al. [75] designed a two-rolling piston expander and tested the expander in a transcritical CO_2 cycle. In a range of rotation speed from 850 to 1000 RPM, the expander achieved an isentropic efficiency of 28-33%. In another study carried out by Hu et al. [76], a two-rolling piston expander prototype was developed and tested in a CO_2 transcritical heat pump system. The expander achieved a maximum efficiency of 77% at the rotation speed of 867 RPM.

2.8.8 Free-Piston Linear Expander

The free-piston linear expander (FPLE) is a positive displacement machine that converts thermal energy directly into electrical energy. It has been a subject of research in recent years and a few design alternatives are proposed in the literature [78-83]. In its traditional design, the FPLE consist of a piston that is free to move within a bore from TDC to BDC without a mechanical linkage, unlike the typical design of the reciprocating piston expander. One of the compact designs is considered to be the free-piston with double-piston structure [79] or, in another words, a piston with two chambers structure [6,77,78]. It consists of a piston with two chambers and a cylinder with four ports, two of which are intake ports and the others are exhaust ports. The cylinder housing has an electric coil. The piston has two chambers connected to each other with a rod, to which permanent magnets are coupled. In each chamber, there are intake and exhaust ports. Figure 2.21 illustrates an example of a piston with two chambers structure of a FPLE. It should be noted that the FPLE design in Figure 2.21 does not use control valves to control the opening of the intake and exhaust ports [6,77,78], unlike other designs [79].

The FPLE, designed by Bonar [6], was designed in such a way that the port of the first chamber of the piston is aligned with the intake port of the cylinder while the port of the second chamber of the piston is in exhaust position, and vice versa. The pressurized working fluid enters the first chamber, creating high-low pressure differential between the two chambers. The piston starts moving in one direction until the second chamber is aligned with intake port of the cylinder and the first chamber is positioned in the exhaust port of the cylinder. The depressurized fluid in the first chamber is then discharged from the exhaust port while the pressurized fluid enters the second chamber of the piston via the intake port of the cylinder. The pressure differential is now created in the opposite direction, directing the piston to move in the opposite direction. When the depressurized fluid in the second chamber reaches the exhaust port, the fluid is pushed out and the pressurized fluid enters the first chamber of the piston through the intake port of the cylinder, completing one cycle. As the piston reciprocates, the magnets coupled to the connecting rod create a magnetic field in the electric coils coupled to the cylinder housing, which is converted into electricity [6].

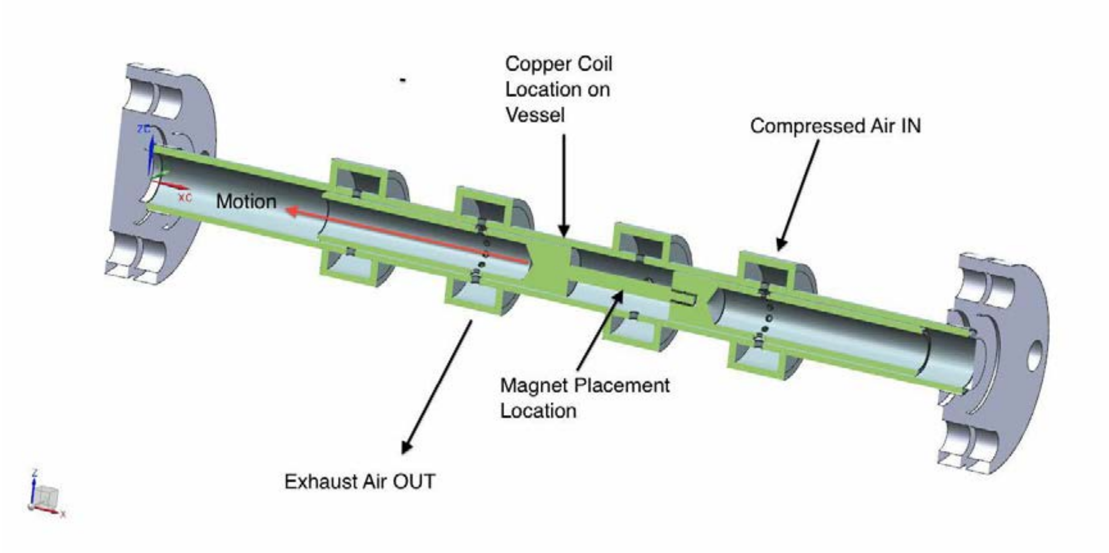

Figure 2.21: Cut-away View of a FPLE [77]

One of the major advantages of this expander is its simple and low manufacturing cost. The expander also has only one moving part, the piston, since the intake and exhaust ports are valveless. On the other hand, the major contributions to the performance losses are due to the friction between the piston and the cylinder wall, heat loss from the cylinder, and the internal leakages between the piston and the cylinder walls.

Nuszkowski et al. [78] modelled and tested a FPLE to analyze the performance of the expander using air as the working fluid. The expander did not succeed in running for periods over ten minutes and due to the electrical generator operating without a load, the isentropic efficiency of the system was zero. However, they achieved a maximum isentropic efficiency of 42% from the parametric study. Hawn et al. [77] designed and tested a FPLE that involved several changes from the expander tested previously by Nuszkowski et al. Air was used as the working fluid. However, the expander failed to achieve the desired steady-state operation due to the seizing of the piston inside the cylinder housing.

Wang et al. [79] conducted an experimental study of a dual-piston air-driven free-piston linear expander coupled with a linear electric generator. In their conceptual design, the air flow into and out of the system was managed by using intake valve and electro-magnetic exhaust valve in each cylinder. They investigated the operational characteristics of the FPLE, which included the piston dynamics, output voltage, operation frequency, and system energy conversion efficiency, at a driven air pressure range between 2-3.75 bar. It was concluded that the expander reached to higher frequency and system energy conversion efficiencies as the driven air pressures increased. The authors also stated that the configuration of the FPLE, compared to the conventional expansion machines, presents significant benefits, such as compact design, low frictional loss, high efficiency, and good operational flexibility [79].

Zhang et al. [80] developed a design of a double acting free piston expander to recover the work in the throttling process of the transcritical CO_2 cycle. A slider-based inlet/outlet control scheme was used to ensure the proper suction, expansion, and discharge processes during operation. The expander was experimentally validated and showed stable operation in a wide range of pressure differences between the inlet and outlet conditions. The optimal working frequency range was observed to be between 10 to 17 Hz and the isentropic efficiency of 62% was achieved from the p-V diagram.

Preetham and Weiss [81] designed a small-scale free piston expander based on a sliding-piston architecture and investigated its operation to use in the conversion of low temperature waste heat sources into useful power output. The control variables were chosen as piston mass, input heat rate, duration of heat input, and external load. The output conditions and trends such as efficiency, operating frequency, and output power were evaluated to identify optimal performance characteristics. It was observed that increasing the heat inputs into the expander resulted in an increase in the power output while decreasing the operating frequency. From the results, the expander efficiency was concluded to be dependent on design parameters, mainly the piston mass and heat input rate.

Champagne and Weiss [82] constructed a millimeter scale free piston expander to use in the low temperature waste heat recovery and its operational parameters were examined to characterize and optimize the piston motion. The optimized parameters included piston sealing, lubrication, piston length, FPE cross sectional area, and input pressure. The results indicated that as the viscosity of the lubricant increased, more efficient sealing was achieved in static environments. The thinner lubricants increased sealing in dynamic motion of the piston.

Li et al. [83] proposed to recover waste heat from vehicle engines by using a novel free-piston expander-linear generator integrated unit. The unit consisted of two free piston expanders and a linear generator connected to each other with piston rods and flexible joints. The intake and exhaust processes of the expander were controlled by mechanical control valve trains driven by servo motors, and the dynamic characteristics of the in-cylinder flow field during the gas inlet-outlet processes were analyzed by using 3-D numerical simulation models. The results indicated that the expander was capable of achieving an efficiency of 66.2% and produce a maximum electrical power output of 22.7 W when the working frequency and intake pressure were 3 Hz and 0.2 MPa, respectively.

2.8.9 Comparison of Expanders

Each expander has advantages and disadvantages depending on several criteria such as its operational limitations, performance, reliability, cost, and noise. Therefore, several parameters need to be evaluated when selecting an expander. Considerations of each type of expanders are presented in summary below.

Turbomachinery: Turbines have a good reputation for high isentropic efficiency and reliability at large scale power generation systems. At small-scale power generation, however, they require excessively high speeds to operate efficiently as the machine size gets smaller. They are also not tolerant of wet expansion and have complicated designs and high manufacturing costs. They are able to achieve isentropic efficiencies as high as 85%, but limited number of studies exists in the literature for small scale power generation.

Scroll Expander: The scroll expanders have been extensively tested in the literature and are commonly used in a variety of applications. The most crucial factor affecting the performance is the leakage. They have complicated geometry and require strict manufacturing tolerances. The scroll expanders are able to operate with wet fluid and have shown isentropic efficiencies as high as 89% in small scale power generation systems.

Screw Expander: The screw expanders have complicated rotor geometry, but robust design. The main challenge of this expander type is sealing which can be assured with oil injection. They are able to handle operations at very high pressure with isentropic efficiencies as high as 76% in small scale power generation systems.

Rotary Vane Expander: This type of expanders has a simple and robust design, and low manufacturing cost. They are capable of handling high operational pressures and have high tolerances of wet expansion. Friction and leakage are the major performance losses.

The rotary vane expanders are able to achieve isentropic efficiencies as high as 73%, but studies on this type of expanders are in limited number in the literature.

Gerotor Expander: In gerotor expanders, both the housing and the rotor rotate and they have complex, but robust design. It can handle high pressures and wet expansion. A relatively low rotational velocity between the rotor and stator provides the advantage of lower friction loss. It is recorded that the gerotor expander was able to achieve an isentropic efficiency of 85%. However, they have not been extensively researched in the literature.

Reciprocating Piston Expander: This expander has a robust design, but is subjected to high frictional losses due to the large contact surfaces. It requires precise valve timing, and vibrations may occur if the structural balance is not assured. They are able to achieve isentropic efficiencies up to 70%, but no literature was found on their performance in an ORC.

Rotary Piston Expander: The rotary piston expander has a simple and robust design, and low manufacturing cost with few parts. It is able to handle high pressure. The main challenge of this expander is to reduce friction and leakage between the piston and the cylinder wall. It has been documented to have an isentropic efficiency of 77%. However, there are a limited number of studies on their performance in an ORC in the literature.

Free-Piston Linear Expander: The configuration of FPLE involves several advantages over conventional expansion machines, such as compact and simple design, low manufacturing cost, good operational flexibility, and high efficiency. Friction and leakage are assumed to be prominent factors on its performance. Another contribution to performance losses is a possible heat loss which can be minimized with proper insulation techniques. In addition, structural balancing is required to prevent excessive vibrations.

Research and development studies on FPLE exist in limited number in the literature. Only one study presents the electrical performance by the free-piston linear expander [79].

Many studies have been observed on conventional expansion machines in the literature. Although the FPLE has a simple design and low manufacturing cost, a limited number of experimental studies on this expander exists in the literature. For this reason, the objective of this study was to develop a FPLE to investigate its performance for use in low temperature energy recovery systems.

3 Experimental Setup and Analysis

The objective of this work was to investigate the performance of the FPLE and to analyze its viability for low temperature heat recovery systems. Heat sources such as waste energy, solar power, and geothermal energy can be utilized to drive the selected expander. However, as aforementioned, a limited number of experimental studies of the FPLE were found in the literature. For this reason, primary attention was focused on the initial operation of the FPLE. For this study, the testing was performed at the University of North Florida's College of Computing, Engineering & Construction's Mechanical Engineering Energy Efficiency Laboratory by using the air as the working fluid provided by means of a compressor. In order to analyze the performance of the FPLE and to compare it with other expander types in the literature, a test bench was developed with measurement devices such as pressure and temperature sensors, LabJack U12, and flow rate meter. The schematic of the testing configuration is shown in Figure 3.1. Below is a brief explanation of the expander design, equipment, measurement devices, and the method of thermodynamic analysis.

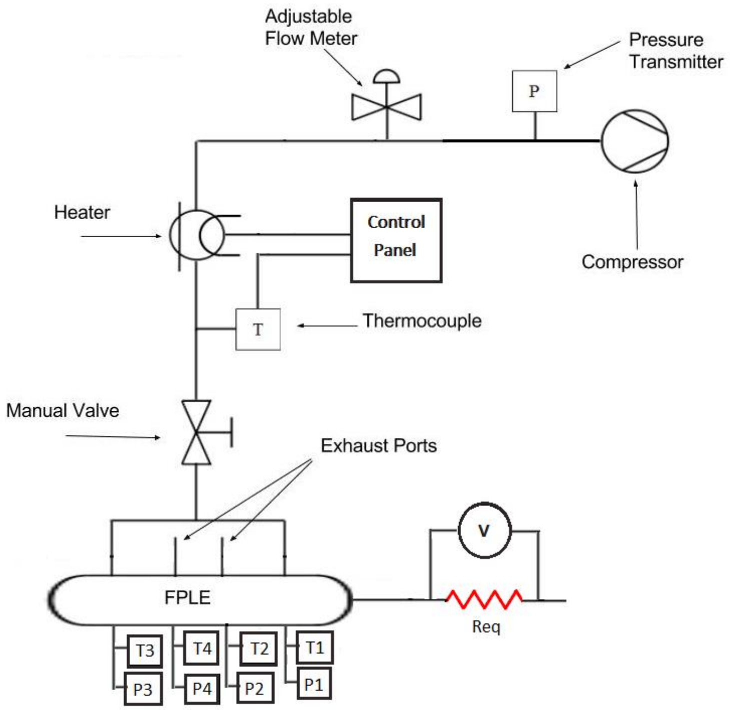

Figure 3.1: Schematic of the Test Bench

3.1 Design

The design of the FPLE was originally proposed to be integrated into an ORC [6]. In this study, the ORC was eliminated from the test bench, as was done in previous studies [77,78], since the primary focus was to achieve a long-term operation of the FPLE. The basic design of the expander contains a free piston that has two independent chambers and reciprocates inside a cylinder housing via compressed air. In spite of the ORC elimination, the FPLE and testing bench was still designed to simulate an ORC implementation [77].

3.1.1 Previous Design

The FPLE in the previous design (see Figure 2.21) was proposed to work as a part of an ORC. The operation resembles the working principles of an engine without the need of a crankshaft, and the method of producing electrical power from the linear motion of the piston is performed by means of magnets coupled to the piston and a coil lined to the cylinder. During its operation, the parameters in each chamber change simultaneously and electrical power is produced as one chamber expands while the other chamber compresses. This process is briefly described in Table 3.1 below.

Table 3.1: Chamber-to-Chamber Working Processes

Process	Left Chamber	Right Chamber
1 → 2	Air Discharge	Air Suction
2 → 3 (Power Extraction)	Compression	Expansion
3 → 4	Air Suction	Air Discharge
4 → 1 (Power Extraction)	Expansion	Compression

The working fluid in an ORC is an organic fluid that is pressurized and then vaporized before entering the expander. However, air was chosen as the working fluid in the previous study [77]. To simulate the expander as a part of an ORC, the organic fluid was modeled. The pressures and the fluid flow rate determined from the parametric model were kept consistent with the use of air. Therefore, the operation of the FPLE was simulated as it would operate in an ORC with an organic fluid. The expander was proposed to generate 60 W and to show an isentropic efficiency of 60% with the following assumptions [77]:

- Air is considered as an ideal gas
- Heat loss is negligible
- The piston is perfectly sealed

- The magnet weight in the piston void is the same as if the void is filled with aluminum

3.1.2 Modifications

Several issues in the previous design were addressed to enhance the performance of the FPLE. Amongst those, the major attention was paid to frictional losses and sealing issues. The leakage was foreseen to occur due to the gap between the piston and the cylinder wall and also in the flange connections of the cylinder. These gaps would cause the leakage of the inlet fluid to both chambers while one of the chambers needs to exhaust the expanded fluid. Leakage due to the gaps would also be caused by air moving from one chamber to another of the piston since the two zones were not sealed in the design. Besides the fact that the leakage would cause a loss in the mass flow rate, thereby in the performance, the primary issue would be the pressure differences between the zones not being created as required and hindering the movement of the piston inside the cylinder. The gaps in the flange connections of the cylinder, on the other hand, will cause the leaking of the air from inside of the cylinder to the environment, adversely affecting the performance of the expander.

Three silicone rubber O-rings on each chamber of the piston (six in total) were used to manage the fluid flow as desired. These rings enhanced the sealing between the cylinder wall and the piston, and also separated the two zones to provide sealing between the two chambers. The reasons for choosing the silicone rubber O-rings are their resistant to high temperatures up to 260 °C and hardness characteristics with a durometer of 70A. However, it was known that the use of three O-rings would increase the contact surface which leads to increased friction. For this reason, a multi-purpose synthetic grease resistant to temperatures up to 232.2 °C was used on the O-rings to reduce the friction. The chosen O-rings had a width, inner diameter and outer diameter of 0.07", 0.926", and 1.066", respectively. According to these dimensions, the grooves on the piston were machined for the O-rings to be placed with a width and depth of 0.1" and 0.054", creating a squeeze ratio of 10% and inner diameter stretch ratio of 1% for the O-rings. The locations of the O-rings were determined in such a way that the air would only fill one chamber while being discharged from the other and vice versa. The piston, with the O-rings located within their grooves, is shown in Figure 3.2.

Figure 3.2: The Piston with O-rings (O-rings in red color)

Another consideration was made to preclude the over-traveling of the piston inside the cylinder. Therefore, a spring-washer cap assembly for each end of the cylinder housing was designed and manufactured to prevent over-traveling during operation. With over-traveling, the piston can be jammed inside the cylinder. The spring-washer caps were attached to the flanges at each end so that the piston would stop at the desired inlet and outlet port locations by hitting the assembly. Spring specifications are shown in Table 3.2. In order to attach the spring-washer caps to the flanges, groves were machined on the flanges with an inner and outer diameter, and depth of 0.48", 0.75", and 0.135", respectively. Using steel as the material, a washer cap was designed, as shown in Figure 3.3, and machined for each spring. The connection between the washer cap and the spring was provided by taking advantage of the friction between the spring and the washer cap.

Table 3.2: Spring Technical Specifications [84]

Spring Type	Compression
Material	Zinc-Plated Music-Wire Steel
End Type	Closed and Flat
Overall Length	1.25"
OD	0.75"
ID	0.48"
Wire Diameter	0.135"
Wire Shape	Round
Compressed Length	0.93"
Maximum Load	134.98 lbs.
Rate	420.50 lbs./in.
RoHS	Compliant

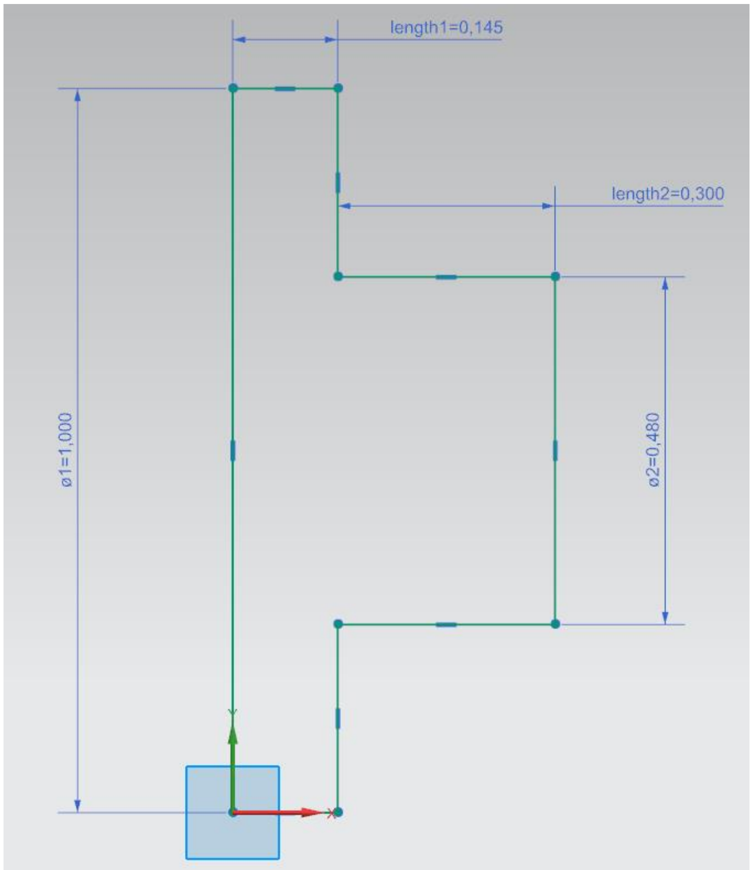

Figure 3.3: 2-D Drawing of the Washer Cap with Dimensions

The sealing at the flange connections of the cylinder was provided via the use of silicone rubber O-rings with the width, inner diameter, and outer diameter of 0.210", 1.475", and 1.895", respectively. According to the O-ring's dimensions, an additional groove on each flange was machined with an inner and outer diameter, and depth of 1.505", 1.925", and 0.146", respectively, creating a squeeze ratio of 30% and inner diameter stretch ratio of 2% for the O-Rings. The Figure 3.4 presents one of the flanges with O-ring and spring-washer cap assembly located in their grooves.

Figure 3.4: The Flange of the Cylinder with O-ring and the Spring-Washer Cap Assembly

Due to inadequate heating and restriction in the flow rate, the heater used in the previous design was replaced with AHP-7561 in-line air heater. The AHP-7561 in-line air heater was capable of providing 750 W with a maximum volumetric flow rate of 20 cfm and was used to heat the air before entering to the FPLE. Table 3.3 presents the technical specification of the AHP-7561.

Table 3.3: Heater Technical Specifications [85]

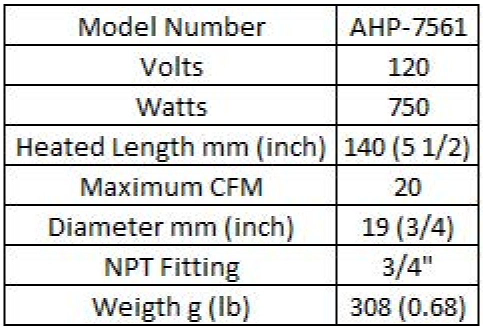

Model Number	AHP-7561
Volts	120
Watts	750
Heated Length mm (inch)	140 (5 1/2)
Maximum CFM	20
Diameter mm (inch)	19 (3/4)
NPT Fitting	3/4"
Weigth g (lb)	308 (0.68)

To reduce the heat being released to the environment during the operation of the FPLE, the cylinder vessel and the inlet air pipeline were insulated with a fiberglass insulation material. The technical specifications of the insulation material are shown in the Table 3.4 below.

Table 3.4: Technical Specifications of Insulation Material [86]

Insulation Type	Tube
Wall Thickness	1"
Temperature Range	0° to 850° F
Jacket Temperature Range	-20° to 150° F
R Value	4.3
Heat Flow Rate	0.23 @ 75° F
Density	4.5 lbs./cu. ft.
Material	Fiberglass
Jacket Material	Kraft Paper/Fiberglass/Foil
Flexibility	Rigid
Tube Style	Slit
Jacket Closure Type	Adhesive Strip
For Use Outdoors	No
Specifications Met	ASTM C547, ASTM C585, ASTM E84 25/50 for Flame and Smoke

It was also observed in the previous study that there was no load attached to the coils wrapped around the middle of the cylinder vessel. Therefore, even if operation was achieved, there would be no electrical power output. For this reason, a resistor bank was established with six resistors of equivalent magnitude in parallel. There were four different resistance magnitudes. Having six resistors at magnitudes of 4 ohm, 10 ohm, 20 ohm, and 50 ohm in parallel made it possible to run the FPLE under an equivalent resistance magnitude of 0.667, 1.667, 3.333, and 8.333 ohm, respectively.

In addition, several clamps were used to clamp the complete experimental setup to the table in order to reduce the vibration during the operation. The Figure 3.5 presents the modified complete system.

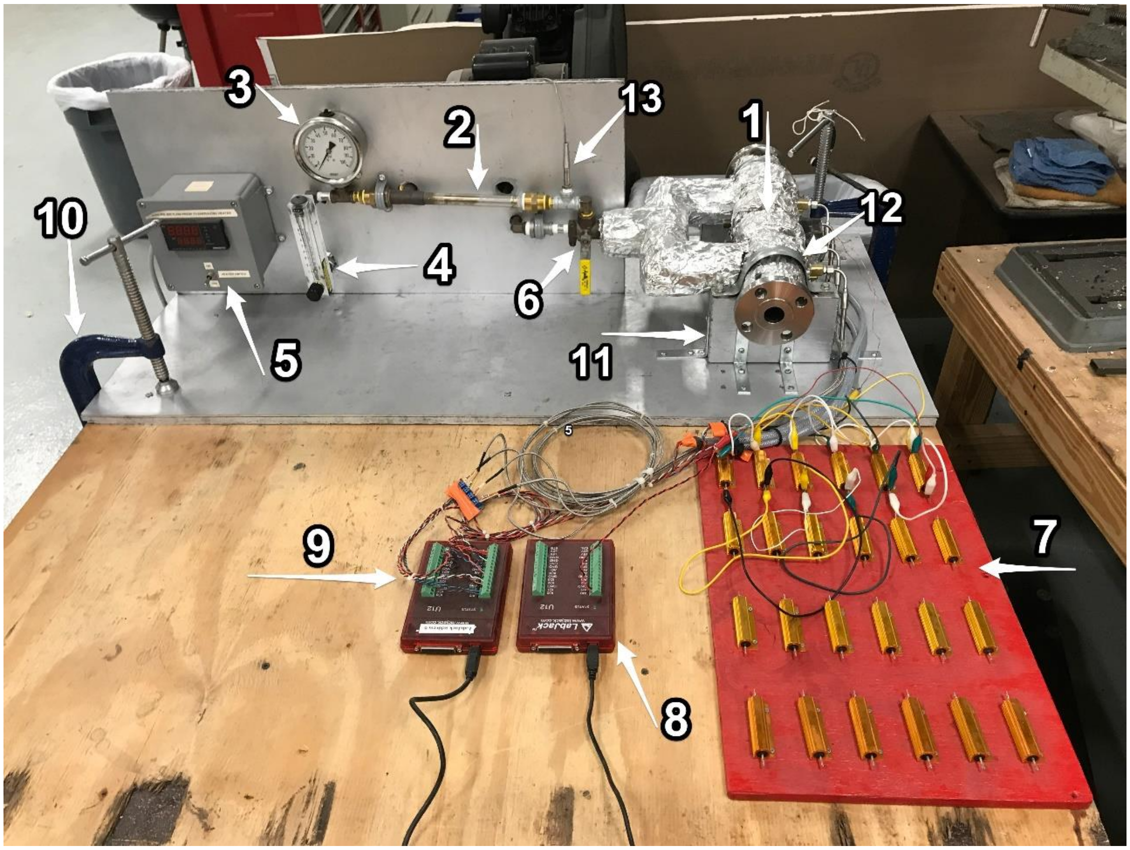

Figure 3.5: FPLE Modified Experimental Setup; 1) FPLE, 2) Heater, 3) Pressure Gauge, 4) Flow Meter, 5) Control Panel, 6) Flow Control Valve, 7) Resistor Bank, 8) LabJack for Voltage Measurements, 9) LabJack for Temperature and Pressure Measurements, 10) C-Clamp for Table, 11) L-Clamp for Expander Support, 12) Pipe Clamp for FPLE, 13) Inlet Air Temperature Thermocouple

3.2 Measurement Devices

Once the initial operation and a steady state operation of the FPLE were achieved, several measurement devices were required for the calculations of the equations presented in Section 3.3. In order to conduct a performance analysis of the FPLE, the parameters necessary to be measured were the inlet and outlet temperatures, inlet and outlet pressures, flow rate, and voltage output.

3.2.1 Temperature Measurements

K-type thermocouples were used to measure the temperatures of the inlet air and the inlet and outlet temperatures of the FPLE's chambers. The inlet air temperature thermocouple was wired to the control panel where a user adjusted the temperature inlet as desired. Therefore, the control panel enabled experiments to be operated at different inlet air temperatures as planned in the design of experiments. In addition, four thermocouples were attached to the inlet and outlet ports of both chambers of the FPLE and connected to the LabJack U12 device (see 3.2.1.4. LabJack U12) in order to measure the inlet and outlet chamber temperatures of the FPLE. Table 3.5 presents the technical specifications of the thermocouples.

Table 3.5: Technical Specifications of the Thermocouples [87]

Operating Temperature	-100 – 1250 °C
Probe Material	Stainless Steel
Probe Diameter	5mm
Probe Length （L）	80mm
Probe Length （L1）	30mm
Standard Limits of Error	Greater of 2.2 °C or 0.75%
Threads Size	1/8” NPT
Threads Lock	Adjustable Pressure Lock
	(Adjustable Length)
Cable Length	2m
Cable External Shielding	Stainless Steel Braiding
Cable Internal Insulation	Fiberglass
Response Time	28 sec

3.2.2 Pressure Measurements

The pressure gauge of Husky air compressor C301H was used to monitor the inlet air pressure supplied to the system, see Table 3.6 for its specifications.

Table 3.6: Specifications of the Pressure Gauge [88]

Pressure Range	0 psi - 300 psi
Product Depth (in.)	3.75
Product Height (in.)	6.75
Product Width (in.)	3.75
Product Weight (lb.)	0.37

Additionally, four gauge pressure sensors were attached to the inlet and outlet ports of both chambers of the FPLE and connected to the LabJack U12 device (see 3.2.1.4. LabJack U12) to measure the inlet and outlet chamber pressures of the FPLE. The technical specifications of the gauge pressure sensor are shown in Table 3.7 below.

Table 3.7: Technical Specifications of the Pressure Sensors [89]

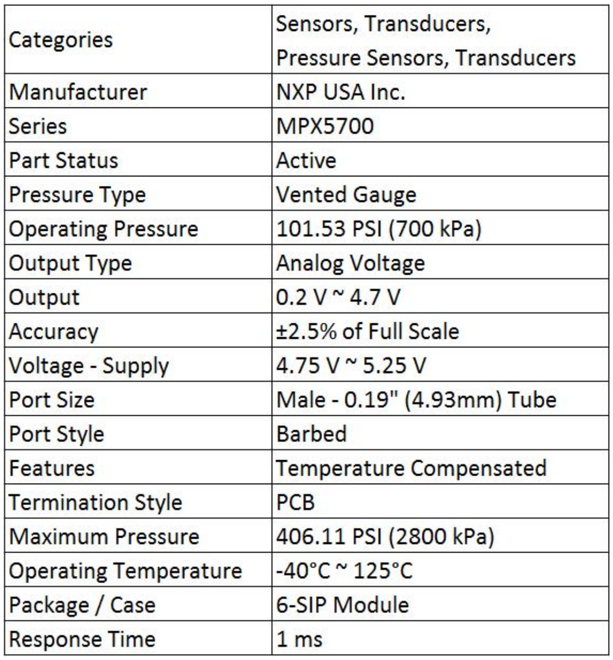

Categories	Sensors, Transducers, Pressure Sensors, Transducers
Manufacturer	NXP USA Inc.
Series	MPX5700
Part Status	Active
Pressure Type	Vented Gauge
Operating Pressure	101.53 PSI (700 kPa)
Output Type	Analog Voltage
Output	0.2 V ~ 4.7 V
Accuracy	±2.5% of Full Scale
Voltage - Supply	4.75 V ~ 5.25 V
Port Size	Male - 0.19" (4.93mm) Tube
Port Style	Barbed
Features	Temperature Compensated
Termination Style	PCB
Maximum Pressure	406.11 PSI (2800 kPa)
Operating Temperature	-40°C ~ 125°C
Package / Case	6-SIP Module
Response Time	1 ms

3.2.3 Flow Rate Measurement

A panel-mount flow meter (Table 3.8) was used to measure the flow rate entering and exiting the expander. This flow meter was also manually adjustable, allowing flow rate control of the system for the experiments operated at different inlet flow rates, as planned in the design of experiments.

Table 3.8: Technical Specifications of the Flow Meter [90]

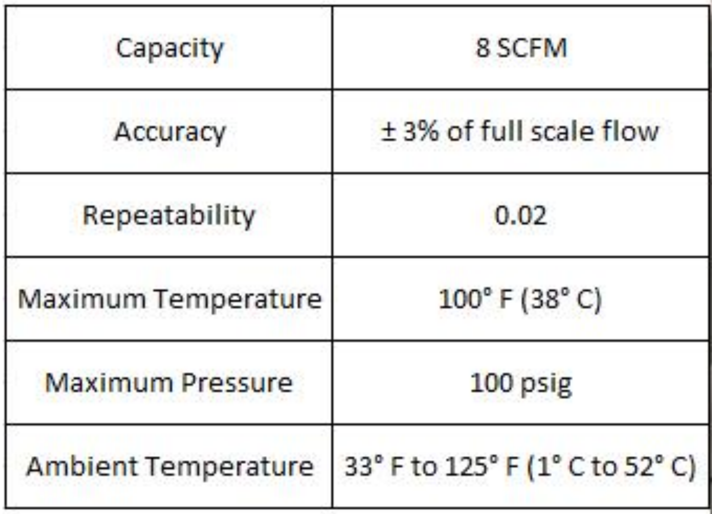

Capacity	8 SCFM
Accuracy	± 3% of full scale flow
Repeatability	0.02
Maximum Temperature	100° F (38° C)
Maximum Pressure	100 psig
Ambient Temperature	33° F to 125° F (1° C to 52° C)

3.2.4 LabJack U12

Two LabJack U12 devices were used in this study. One was connected to the thermocouples and the pressure sensors that are attached to the FPLE chamber inlet and outlet ports to measure the chamber inlet and outlet temperature and pressure values. The temperature and pressure values were displayed and recorded using LJLogger software of LabJack U12 device, and used in the performance analysis.

The other LabJack U12 was connected to the electrical circuit of the FPLE to display and measure the voltage outputs during operation. LJScope software of the LabJack U12 device was used to record the voltage measurements in order to calculate the frequency, electrical power output, and mechanical-electrical conversion efficiency. The analog input technical specifications of the LabJack U12 are shown in the Table 3.9 below.

Table 3.9: Analog Inputs (AI0 – AI7) Technical Specifications of the LabJack U12 [91]

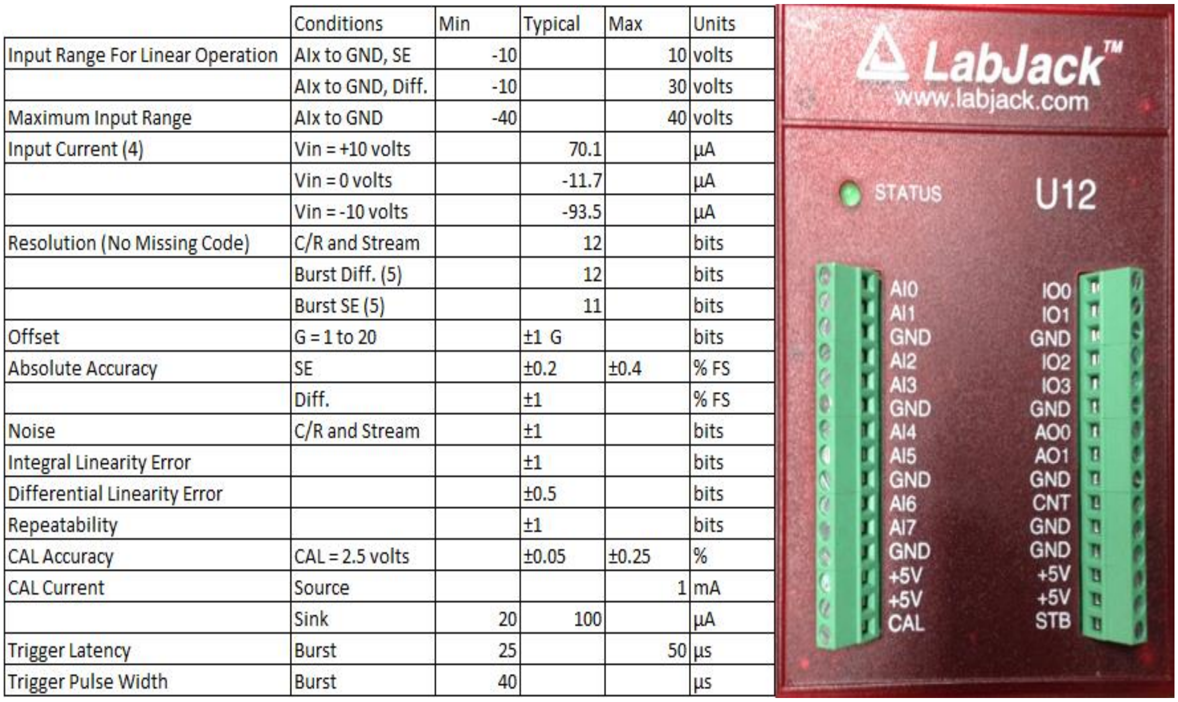

	Conditions	Min	Typical	Max	Units
Input Range For Linear Operation	AIx to GND, SE	-10		10	volts
	AIx to GND, Diff.	-10		30	volts
Maximum Input Range	AIx to GND	-40		40	volts
Input Current (4)	Vin = +10 volts		70.1		µA
	Vin = 0 volts		-11.7		µA
	Vin = -10 volts		-93.5		µA
Resolution (No Missing Code)	C/R and Stream		12		bits
	Burst Diff. (5)		12		bits
	Burst SE (5)		11		bits
Offset	G = 1 to 20		±1 G		bits
Absolute Accuracy	SE		±0.2	±0.4	% FS
	Diff.		±1		% FS
Noise	C/R and Stream		±1		bits
Integral Linearity Error			±1		bits
Differential Linearity Error			±0.5		bits
Repeatability			±1		bits
CAL Accuracy	CAL = 2.5 volts		±0.05	±0.25	%
CAL Current	Source			1	mA
	Sink	20	100		µA
Trigger Latency	Burst	25		50	µs
Trigger Pulse Width	Burst	40			µs

3.3 Thermodynamic Analysis

Thermodynamic analysis of the FPLE was necessary to investigate its performance. The analysis was carried out by using the first and second laws of thermodynamics. Conservation of mass, energy, and entropy were applied to analyze the performance of the expander. The cylinder vessel of the FPLE was taken as the control volume for the analysis, which has two inlets and outlets.

The conservation of energy for the control volume is:

$$\frac{d\mathrm{E}_{cv}}{dt} = \dot{Q} + \dot{W} + \dot{m}_{in}\left(h_{in} + \frac{V_{in}^2}{2} + gz_{in}\right) - \dot{m}_{out}\left(h_{out} + \frac{V_{out}^2}{2} + gz_{out}\right) \tag{1}$$

where $\frac{d\mathrm{Ecv}}{dt}$ is the rate of change in total internal energy (W), $\dot{Q}$ is the rate of heat transfer (W), $\dot{W}$ is the power output of the expander (W), $\dot{m}_{in/out}$ is the mass flow rate of inlet and outlet (kg/s). $h_{in/out}$, $V_{in/out}$, and $z_{in/out}$ represent enthalpy, velocity and the height level of the air at the inlet and outlet (J/kg), respectively.

The conservation of mass for the control volume is:

$$\frac{d\mathrm{m}_{cv}}{dt} = \dot{m}_{in} - \dot{m}_{out} \tag{2}$$

The entropy balance and irreversibility equations for the control volume are:

$$\frac{dS_{cv}}{dt} = \dot{m}_{in}s_{in} - \dot{m}_{out}s_{out} + \frac{\dot{Q}}{T_s} + \dot{S}_{gen} \tag{3}$$

$$I = T_s\,\dot{S}_{gen} \tag{4}$$

where $\frac{dS_{cv}}{dt}$ is the rate of change in total entropy of the system, $s_{in/out}$ is the entropy of the air at inlet and outlet, T_s is the temperate of surroundings (equivalent to 293.15 K in this study), and $\dot{S}_{gen}$ is the entropy generated during the expansion process.

The volumetric efficiency of the FPLE can be defined as the ratio of the actual mass flow rate to the mass flow rate of the ideal process. Therefore, during operation, the volumetric efficiency is determined by:

$$\lambda = \frac{\dot{m}_a}{\rho_a V_d f} \tag{5}$$

where λ is the volumetric efficiency, $\dot{m}_a$, ρ_a, V_d, and f represent air mass flow rate supplied into one of the chambers, density of air evaluated at atmospheric conditions, displacement volume, and frequency of the piston motion, respectively.

After a long-enough time, when the readings from the control volume did not change, the operation of the expander can be assumed to be steady state. Therefore, steady state conditions are assumed for this thermodynamic analysis. This assumption simplifies the analysis and the change in any property with respect to time become equal to zero. As is done by the previous study [77], heat losses are assumed to be negligible and the system is assumed to be perfectly sealed. In addition, the changes in kinetic and potential energy are negligibly small values and are equal to zero in this analysis. It was also assumed that the volumetric flow rates into both chambers are equal and half of the total volumetric flow rate. Since the air was considered as ideal gas, enthalpy properties of the air at the inlet and outlet, and the change in the entropy of the air were calculated by the following equations:

$$h = c_p T \tag{6}$$

$$s_{in} - s_{out} = c_p \ln\left(\frac{T_{out}}{T_{in}}\right) - R_a \ln\left(\frac{P_{out}}{P_{in}}\right) \tag{7}$$

where c_p is the specific heat of the air and taken as a constant value, 1.005 kJ/kg-K, T is the temperature of the air. R_a denotes the gas constant of air and taken as constant value, 0.2869 kJ/kg-K. After applying the assumptions into equation (1), (2), and (3) and substituting the equation (6) and (7) into equation (1) and (3), respectively, the following equations were obtained:

$$\dot{m}_{in} = \dot{m}_{out} = 2\dot{m}_{1,in} = 2\dot{m}_{2,out} = 2\dot{m}_{3,in} = 2\dot{m}_{4,out} = \dot{m} = \rho_a \dot{V}_{in} \tag{8}$$

$$\dot{W}_{out,a} = \frac{\dot{m}}{2} c_p \left\{ \left(T_{1,in} - T_{2,out,a}\right) + \left(T_{3,in} - T_{4,out,a}\right) \right\} \tag{9}$$

$$\dot{S}_{gen} = \frac{\dot{m}}{2} \left\{ \left[c_p \ln\left(\frac{T_2}{T_1}\right) - R_a \ln\left(\frac{P_2}{P_1}\right) \right] + \left[c_p \ln\left(\frac{T_4}{T_3}\right) - R_a \ln\left(\frac{P_4}{P_3}\right) \right] \right\} \tag{10}$$

where the subscripts of 1, 2, 3, and 4 represent the states of the right chamber inlet, right chamber outlet, left chamber inlet, and left chamber outlet, respectively. $\dot{V}_{in}$ represents the total volumetric flow rate entering the control volume. $\dot{W}_{out,a}$, $T_{2,out,a}$, and $T_{4,out,a}$ denote actual expander work, and actual temperature at the outlets of the right and left chambers, respectively. Finally, the isentropic efficiency for the control volume can be defined as the ratio of the actual expander work output to the isentropic expander work output:

$$\eta_s = \frac{\dot{W}_{out,a}}{\dot{W}_{out,s}} \tag{11}$$

where η_s is the isentropic efficiency, and $\dot{W}_{out,s}$ is the isentropic work output of the expander which is defined by:

$$\dot{W}_{out,s} = \frac{\dot{m}}{2} c_p \{(T_{1,in} - T_{2,out,s}) + (T_{3,in} - T_{4,out,s})\} \tag{12}$$

where $T_{2,out,s}$ and $T_{4,out,s}$ are the exit temperature of the air at, respectively, right and left chambers for an isentropic expansion process and can be calculated by the following relationship:

$$T_{out,s} = T_{in} \left(\frac{P_{out}}{P_{in}}\right)^{\frac{k-1}{k}} \tag{13}$$

where P_{in} is the inlet chamber pressure, P_{out} is the outlet chamber pressure. The atmospheric pressure in this study was taken as 101.325 kPa, and k is the specific heat ratio and taken as a constant value, 1.401. Moreover, the average electrical power output is calculated by the following relationship:

$$\dot{W}_{e,avg} = \frac{V_{RMS}}{R^2{}_{eq}} \tag{14}$$

where $\dot{W}_{e,avg}$, V_{RMS}, and $R^2{}_{eq}$ represent the average electrical power (W), RMS (root of mean square) voltage (V), and the equivalent resistance (ohm), respectively. The RMS voltage of a sample voltage data set of n value can be calculated using the following relationship:

$$V_{RMS} = \sqrt{\frac{{V_1}^2 + {V_2}^2 + {V_3}^2 + \ldots + {V_n}^2}{n}} \tag{15}$$

Mechanical-electrical conversion efficiency of the FPLE can be defined as the ratio of the electrical power output (average) to the actual expander work. Therefore, during the operation of the FPLE, the mechanical-electrical conversion efficiency, η_c, is defined as:

$$\eta_c = \frac{\dot{W}_{e,avg}}{\dot{W}_{out,a}} \tag{16}$$

After achieving steady state operation of the FPLE, the inlet-outlet relationships were evaluated in order to examine the operational characteristics and to identify the conditions and trends for optimal performance of the FPLE. Table 3.10 presents the design of experiments with the independent and dependent variables.

Table 3.10: Design of Experiments

Test #	**Independent Variable**	**Dependent Variables**	**Controlled Variables**
1	Inlet Air Pressure (Range: 275.8-551.6 kPa in Absolute Units)	Actual Expander Work Irreversibility Isentropic Efficiency Frequency Volumetric Flow Rate Volumetric Efficiency RMS Voltage Electrical Power Output Conversion Efficiency	Inlet Air Temperature Resistance Magnitude
2	Inlet Air Temperature (Range: 50–90 °C)	Actual Expander Work Irreversibility Isentropic Efficiency Frequency Volumetric Efficiency RMS Voltage Electrical Power Output Conversion Efficiency	Inlet Air Pressure Resistance Magnitude Volumetric Flow Rate
3	Resistance Magnitude (Range: 0.667-8.333 Ohm)	Actual Expander Work Irreversibility Isentropic Efficiency Frequency Volumetric Efficiency RMS Voltage Electrical Power Output Conversion Efficiency	Inlet Air Pressure Inlet Temperature Volumetric Flow Rate

3.3.1 Propagation of Error

Uncertainty analysis was performed to provide the accuracies of the calculated parameters since the measurements from multiple instruments were included in the calculation of the parameters. Standard deviations of the calculated parameters were determined by using the exact formula for propagation of error [92]:

$$\sigma_x^2 = \left(\frac{\delta x}{\delta a}\right)^2 \sigma_a^2 + \left(\frac{\delta x}{\delta b}\right)^2 \sigma_b^2 + \left(\frac{\delta x}{\delta c}\right)^2 \sigma_c^2 \tag{17}$$

where x is defined as the parameter desired (e.g., η_s, $\dot{W}_{out,s}$, $\dot{S}_{gen}$, etc.) and is function of a, b, and c. The standard deviations of x, a, b, and c, are represented by σ_x, σ_a, σ_b, and σ_c, respectively.

4 Results and Discussion

The steady state operation of the Free-Piston Linear Expander was successfully achieved after applying the forementioned modifications. The experiments were conducted at the University of North Florida's College of Computing, Engineering & Construction's Mechanical Engineering Energy Efficiency Laboratory in order to analyze the performance of the FPLE by varying the inlet pressure and inlet temperature of the air, and the electrical resistance, connected as the output load to the expander. The thermodynamic and voltage data recordings were started after running each experiment. A range in the temperature readings where the readings were steady was chosen as the steady state region. The average values of the thermodynamic and voltage data in the steady state regions were used as the steady state properties for the analysis of each experiment. The Figure 4.1 presents an example for the selection of the steady state region of an experiment with the inlet air pressure and temperature, and the resistance magnitude of 413.7 kPa, 50 °C, and 0.667 ohm, respectively. The bars labeled with 1500 and 1680 in Figure 4.1 indicates the boundaries of the steady state region. The 1500 and the 1680 labels are the time since the data recording started.

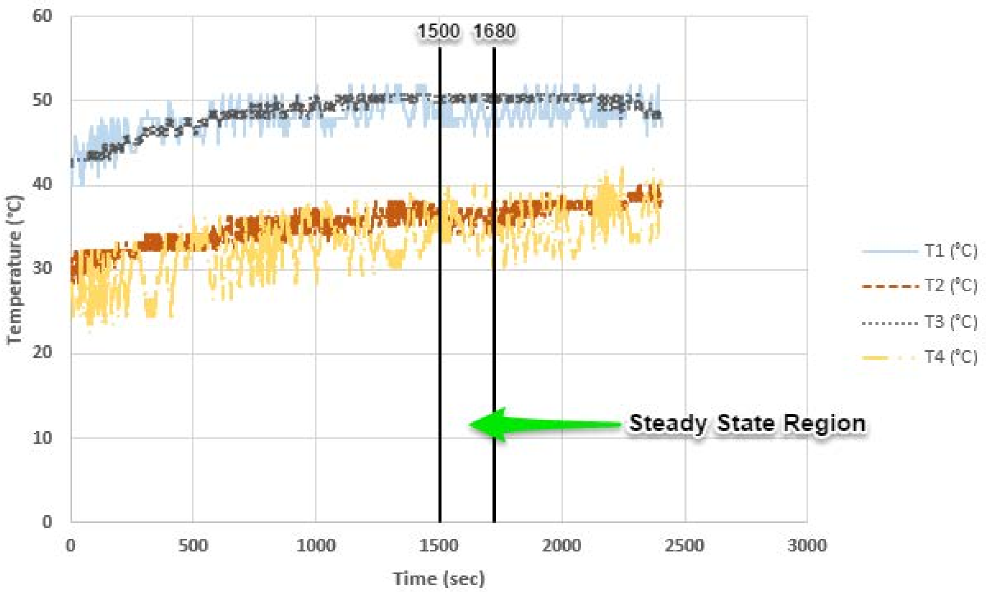

Figure 4.1: Determination of Steady State Region

4.1 Different Inlet Air Pressures

As the initial experimental set, the inlet pressure range was 275.8-551.6 kPa (equivalent to 40-80 psi) with 68.9 kPa (10 psi) increments in absolute units while keeping the inlet air temperature, and the resistance magnitude at 90 °C and 0.667 ohm, respectively. In the second experiment set, the inlet air temperature range was 50-90 °C with 10 °C increments, and the control of the inlet air pressure and the magnitude of the load were 413.7 kPa (60 psi) and 0.667 ohm, respectively. In the last experiment set, the resistance magnitude of the load was varied between 0.667-8.333 ohm while keeping the inlet air pressure and temperature constant at 413.7 kPa (60 psi) and 90 °C, respectively. The thermodynamic and the voltage-time data of the FPLE were collected to determine the isentropic efficiency and the power output. Table 4.1 presents the steady state thermodynamic data collected for five runs with different air inlet pressures.

Table 4.1: Experimental Thermodynamic Data Collected at Different Inlet Air Pressures

	Units	Run 1	Run 2	Run 3	Run 4	Run 5
Inlet Air Pressure	kPa	275.8	344.7	413.7	482.6	551.6
P1 (Left chamber inlet)	kPa	165.7	208.3	260.3	340.2	374.8
P2 (Left chamber outlet)	kPa	0.8	1.8	3.9	6.3	7.0
P3 (Right chamber inlet)	kPa	167.2	207.9	255.4	337.8	373.0
P4 (Right chamber outlet)	kPa	1.6	2.6	3.5	5.3	8.8
T1 (Left chamber inlet)	°C	69.3	75.3	79.7	77.1	80.2
T2 (Left chamber outlet)	°C	55.2	59.6	61.4	59.1	57.6
T3 (Right chamber inlet)	°C	70.4	77.6	78.5	84.2	83.7
T4 (Right chamber outlet)	°C	51.1	55.8	55.2	57.0	54.1
V dot (Air)	m3/s	0.00121	0.00149	0.00177	0.00224	0.00233

It should be noted that the left and right chamber inlet and outlet pressure data collected from the LabJack U12 represent the gauge pressure values. Therefore, the atmospheric pressure of 101.325 kPa was added to the P_1, P_2, P_3, and P_4 measurements in the performance analysis. The voltage-time data collected using LJScope software of the LabJack U12 device.

Based on the steady state thermodynamic and voltage-time data, the performance analysis of the expander at different inlet air pressure values was conducted and the summary was presented in Table 4.2. For each experiment, the average of the RMS voltages from multiple voltage datasets over the steady state range was used in the electrical power output calculation. The frequency of the expander operation was calculated by using the Fast Fourier Transform function in Excel on the voltage-time data at steady state and the results are included in the expander performance summary tables. From the different inlet air pressure experiments, the maximum isentropic efficiency of the

FPLE was observed as 21.5%, producing actual expander work and electrical power of 75.13 W and 3.302 W, respectively.

Table 4.2: The FPLE Performance Summary at Different Inlet Air Pressures

	Units	Run 1	Run 2	Run 3	Run 4	Run 5
Frequency	Hz	30.03	35.03	35.03	37.03	44.01
Average RMS Voltage	V	0.579	0.473	0.817	1.285	1.467
Electrical Power Output	W	1.303	1.064	1.839	2.891	3.302
Actual Expander Work	W	24.99	34.48	45.35	62.34	75.13
Isentropic Expander Work	W	123.05	172.88	228.04	324.51	350.24
Irreversibility	W	98.10	138.76	185.69	272.85	288.97
Isentropic Efficiency	%	20.3	19.9	19.9	19.2	21.5
Mechanical-Electrical Conversion Efficiency	%	5.2	3.1	4.1	4.6	4.4
Volumetric Efficiency	%	73.0	77.0	91.4	109.3	95.8

The frequency is plotted versus inlet air pressure in Figure 4.2. The experimental results clearly showed that the frequency tended to increase as the inlet air pressure increased. It can be anticipated that at higher inlet air pressures and flow rates, the expander frequency will be higher. The increasing expander frequency can be also interpreted as increasing piston reciprocating velocity. It should be noted that the error bars in Section 4, represent the standard deviations of the calculated parameters, as mentioned in Section 3.3.1. The values of the standard deviations are presented in the Appendix A.

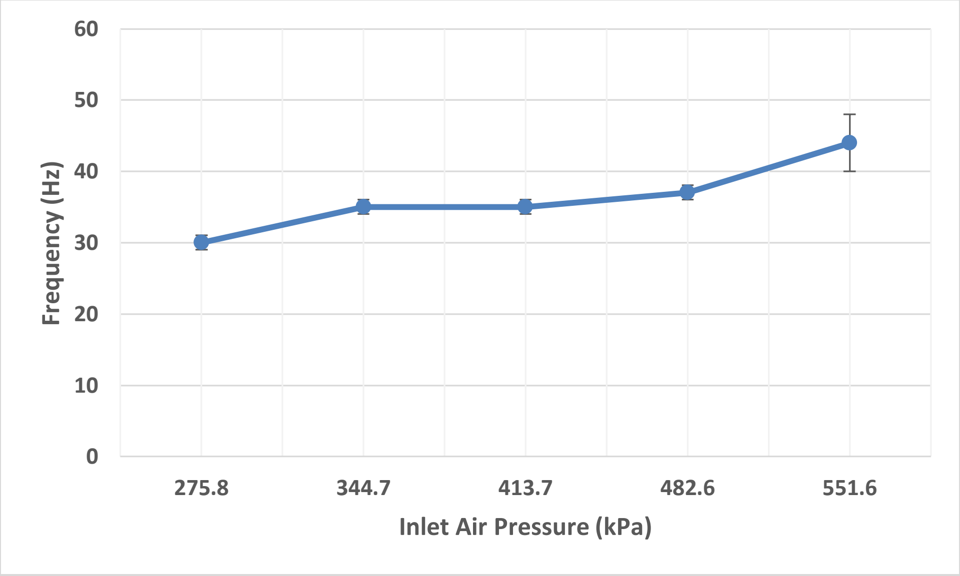

Figure 4.2: Variation in Expander Frequency for Different Inlet Air Pressures

Figure 4.3 presents the different efficiencies at different inlet air pressures. From the experimental results, FPLE showed slightly lower isentropic efficiencies as the inlet air pressure increased, but reached the maximum isentropic efficiency at the highest inlet air pressure of 551.6 kPa. However, the isentropic efficiencies were within the propagation of error, indicating a steady trend at different inlet air pressures. The volumetric efficiency tended to increase as the inlet air pressure increased up to 482.6 kPa where it reached the peak point of 109.3%. Increasing the inlet air pressure from 482.6 kPa to 551.6 kPa then led to a decrease to 95.8% in the volumetric efficiency even though the volumetric flow rate increased at 551.6 kPa. However, this decrease in the experimental volumetric efficiency was within the propagation of error. The results of mechanical-electrical conversion efficiency ranged between 3.1-5.2%, clearly indicating the cause of the high differences between the actual expander work and the electrical power output (Table 4.2).

The RMS voltage output trend at different inlet air pressures is shown in the Figure 4.4. It was observed that the voltage output increased with the increase of the inlet pressure.

The maximum voltage of the different inlet air pressures was achieved as 1.467 V, corresponding to the maximum electrical power output of 3.302 W. It can be anticipated that the voltage output will increase at higher inlet air pressures.

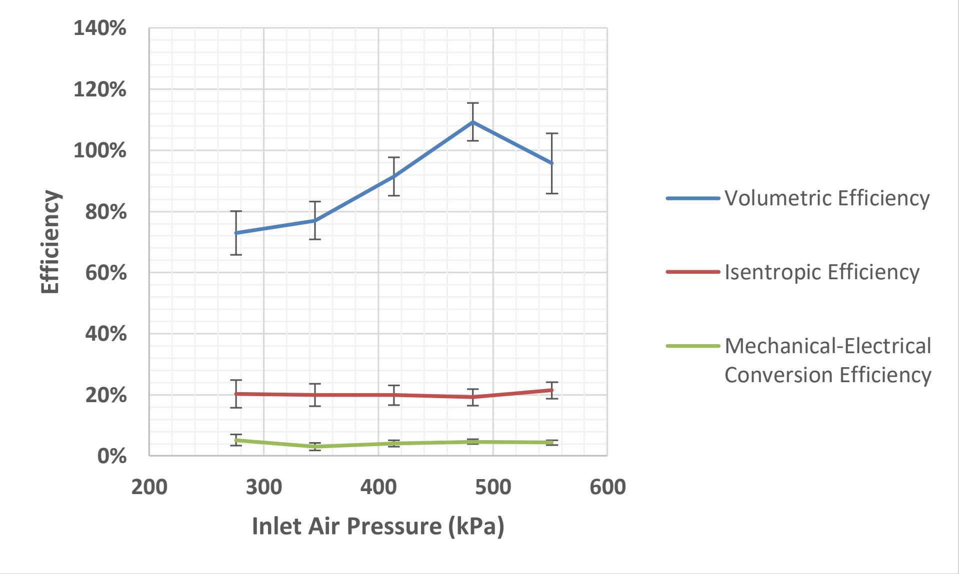

Figure 4.3: Efficiencies at Different Inlet Air Pressures

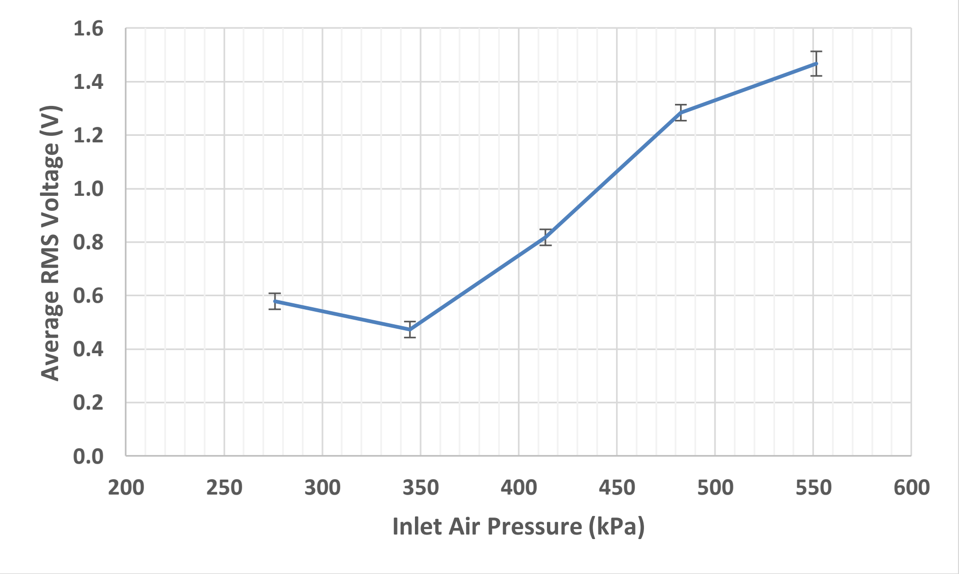

Figure 4.4: The Average RMS Voltages at Different Inlet Air Pressures

Figure 4.5 presents the actual expander work and irreversibility at different inlet air pressures. The actual expander work was higher with higher inlet air pressures even though the isentropic efficiency did not significantly change. This was due to the rate of increase in the irreversibility being the same as the rate of increase in the actual expander work. The most probable reason of the increase in the irreversibility is that the frictional losses increased as the inlet air pressure increased.

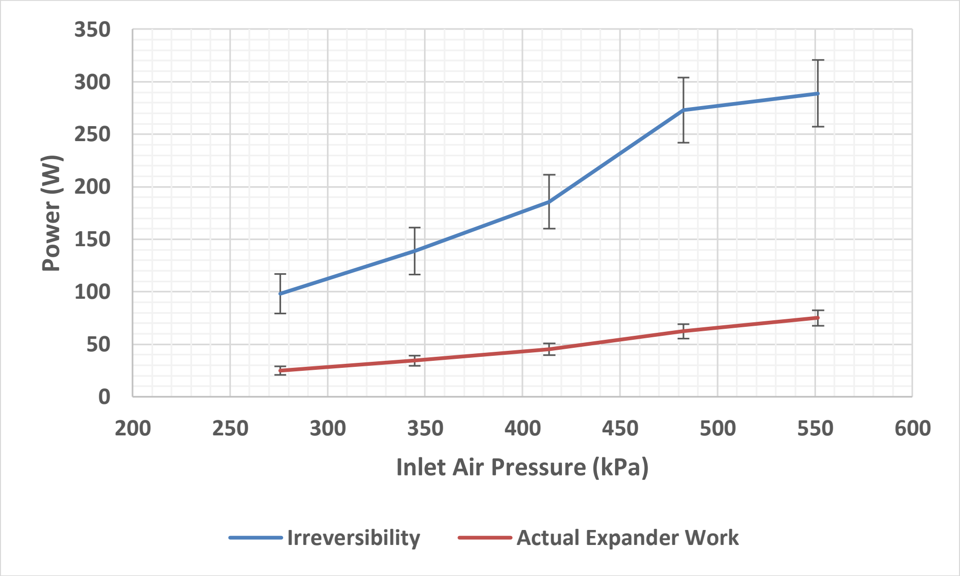

Figure 4.5: Actual Expander Work and Irreversibility Variations in Different Inlet Air Pressures

4.2 Different Inlet Air Temperatures

In the second set of experiments, the independent variable was the inlet air temperature ranging from 50-90 °C with 10 °C increments. The inlet air pressure, the volumetric flow rate and the resistance magnitude were the controlled variables at 413.7 kPa and 0.667 ohm, respectively. The steady state operations of the FPLE at five different inlet air temperature values are presented in the Table 4.3 below.

Table 4.3: Experimental Thermodynamic Data Collected at Different Inlet Air Temperatures

	Units	Run 1	Run 2	Run 3	Run 4	Run 5
Inlet Air Temperature	°C	50	60	70	80	90
P1 (Left chamber inlet)	kPa	250.3	257.1	259.0	255.4	177.9
P2 (Left chamber outlet)	kPa	3.9	2.7	3.7	3.0	7.8
P3 (Right chamber inlet)	kPa	248.2	253.8	258.0	251.7	179.4
P4 (Right chamber outlet)	kPa	4.2	4.0	4.0	4.2	2.6
T1 (Left chamber inlet)	°C	48.4	59.9	65.5	70.2	71.5
T2 (Left chamber outlet)	°C	36.1	44.7	51.8	53.1	63.2
T3 (Right chamber inlet)	°C	50.7	58.5	67.6	73.2	70.4
T4 (Right chamber outlet)	°C	35.2	39.8	48.2	52.6	52.1
V dot (air)	m3/s	0.00170	0.00168	0.00168	0.00168	0.00205

The pressure measurements in Table 4.3 show the gauge pressure of the states. The atmospheric pressure of 101.325 kPa was added to the defined steady state pressure values when analyzing the performance of the FPLE. Comparing to the other experimental runs, lower chamber inlet pressure values and higher volumetric flow rate were measured in the experiment with the inlet air temperature of 90 °C (Run 5). The most probable reason is the internal leakage occurring between the O-rings and the cylinder walls. Based on the thermodynamic data (Table 4.3) and voltage-time data at steady state, the performance analysis of the expander at five different inlet air temperatures was conducted. The results are summarized in Table 4.4 below. The maximum isentropic efficiency of the expander was achieved at 80 °C (Run 4) as 18.6%, producing actual expander work and electrical power 39.03 W and 1.945 W, respectively.

Table 4.4: The FPLE Performance Summary at Different Inlet Air Temperatures

	Units	Run 1	Run 2	Run 3	Run 4	Run 5
Frequency	Hz	35.03	35.03	34.03	34.03	31.03
Average RMS Voltage	V	1.484	1.826	1.455	1.445	0.967
Electrical Power Output	W	1.773	2.478	1.808	1.945	1.133
Actual Expander Work	W	29.00	35.13	34.31	39.03	33.63
Isentropic Expander Work	W	196.88	203.43	208.44	209.93	210.13
Irreversibility	W	184.01	180.47	182.56	176.81	175.17
Isentropic Efficiency	%	14.7	17.3	16.5	18.6	16.0
Mechanical-Electrical Conversion Efficiency	%	6.1	7.1	5.3	5.0	3.4
Volumetric Efficiency	%	87.8	86.6	89.2	89.2	119.5

The frequency plot at different inlet air temperatures can be seen in the Figure 4.6 below. Unlike the frequency trend of the FPLE at different inlet air pressures, the frequency tended to decrease as the inlet air temperature increased. The highest and the lowest values were achieved at 50 °C and 90 °C as 35.03 Hz and 31.03 Hz, respectively. The average RMS voltage trend at different inlet air temperatures is illustrated in Figure 4.7. The maximum average RMS voltage value was achieved at 60 °C as 1.826 V, producing the maximum electrical power of 2.478 W. With further increase of temperature, the average RMS voltage started decreasing, thereby lowering the electrical power output. The trend in the Figure 4.7 shows that the voltage output was likely to decrease at even higher temperatures.

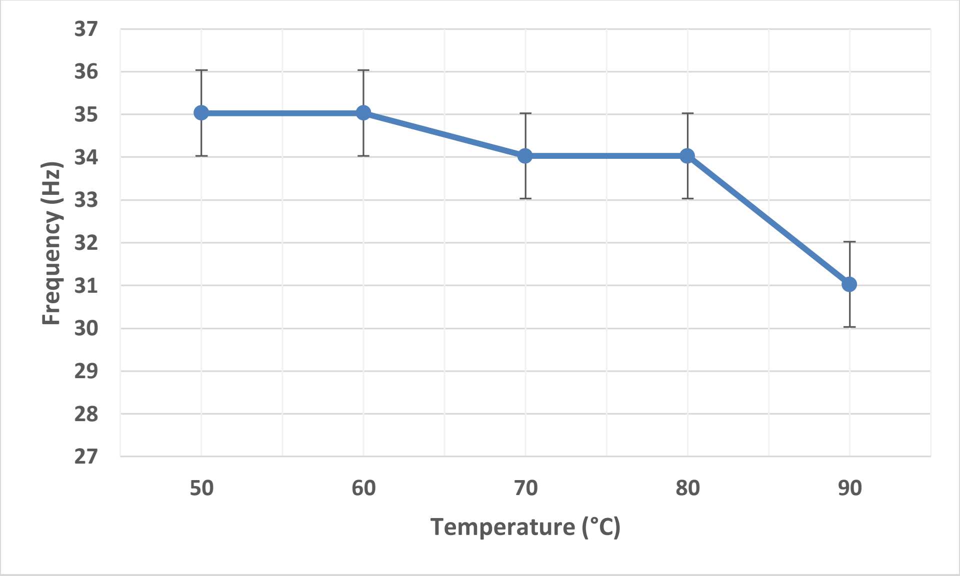

Figure 4.6: Variation of Expander Frequency for Different Inlet Air Temperatures

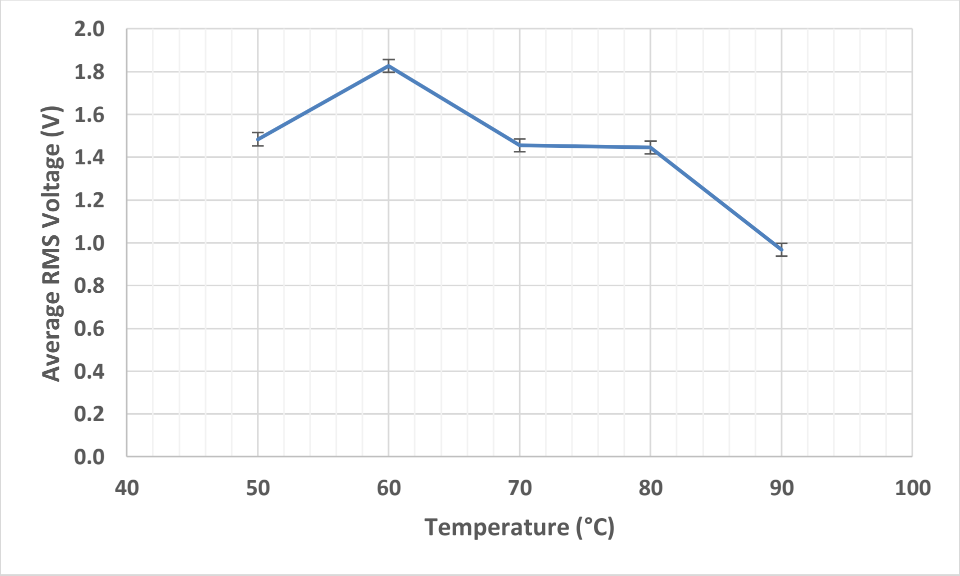

Figure 4.7: The Average RMS Voltages at Different Inlet Air Temperatures

The trends of the efficiencies at different inlet air temperatures are shown in Figure 4.8. For different inlet air temperatures, the isentropic efficiency ranged between 14.7% and 18.6%. The maximum electrical power of 2.478 W was produced during the second run (inlet air temperature of 60 °C) while the isentropic efficiency was 17.3%. The reason for this is that the mechanical-electrical conversion efficiency reached its peak value, 7.1%, for the inlet air temperature of 60 °C, allowing the production of more electric power even though the actual expander work was not at its highest value. In this same experiment, the FPLE showed the lowest volumetric efficiency of 86.6%. With the further increase of the inlet air temperature, the volumetric efficiency was observed to increase, reaching to its highest value of 119.5% at the inlet air temperature of 90 °C. From 50 °C to 80 °C, the volumetric efficiency showed slight changes, which were found to be within the propagation of error. On contrary, at the inlet air temperature of 90 °C, a significant increase in the volumetric efficiency was observed. This can be connected to an excessive internal leakage occurring between the piston O-rings and the cylinder walls, which supports the hypothesis stated previously regarding the low chamber inlet pressures and high volumetric flow rate measurements for the inlet air temperature of 90 °C (Table 4.3). The mechanical-electrical conversion efficiency, on the other hand, tended to decrease as the inlet air temperature increased from 60 °C to 90 °C. Moreover, the trends in Figure 4.8 clearly shows that the volumetric efficiency will likely increase at even higher temperatures, whereas the mechanical-electrical conversion efficiency can be expected to further decrease.

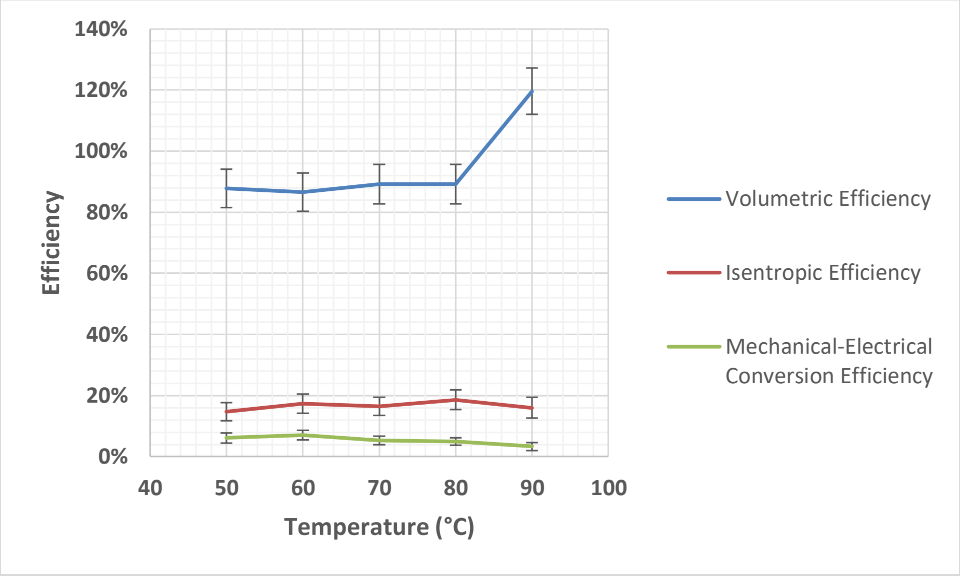

Figure 4.8: Efficiencies at Different Inlet Air Temperatures

Figure 4.9 presents the trends of the actual expander work and the irreversibility of the FPLE at different inlet air temperatures. Actual expander work tended to increase as the inlet air temperature increased, reaching at its peak value of 39.03 W with an inlet air temperature of 80 °C. Increasing the temperature from 80 °C to 90 °C resulted in a decrease in the actual expander work. This was likely due to excessive internal leakage, which also explains why the chamber inlet pressure values were low and the volume flow rate was high for 90 °C. Internal leakage was possible between the O-rings and the cylinder wall that can cause the leaking of air from one chamber to another and/or inlet to outlet. The irreversibility, on the other hand, had a tendency to decrease as the inlet air temperature increased. It can be also seen from Figure 4.9 that the irreversibility was likely to further decrease at even higher inlet air temperatures.

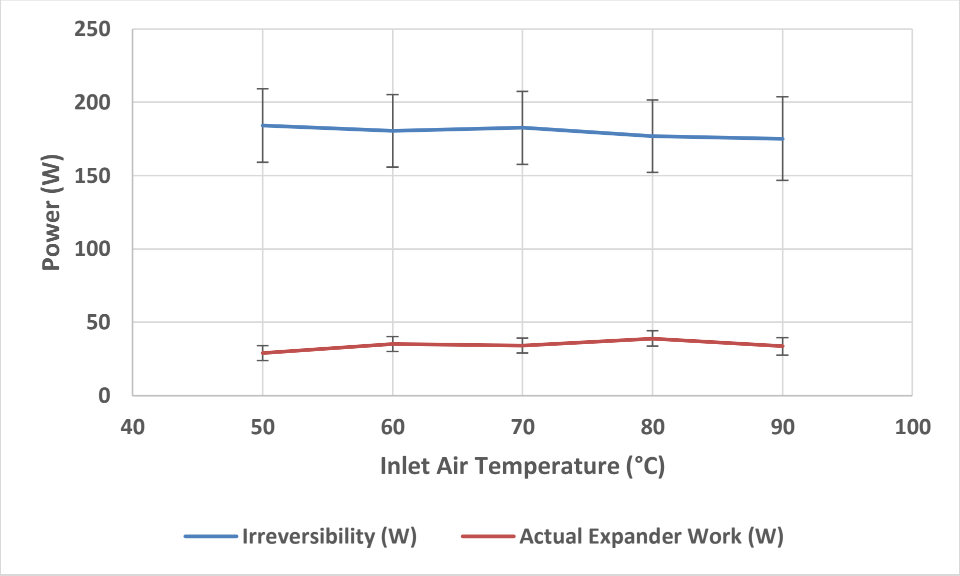

Figure 4.9: Actual Expander Work and Irreversibility Variations in Different Inlet Air Temperatures

4.3 Different Resistance Magnitudes

In the third and last set of experiments, the inlet air temperature and the pressure values were controlled at 90 °C and 413.7 kPa, respectively, while varying the magnitude of the load connected to the FPLE from 0.667 up to 8.333 ohms. Four experiments with different resistance magnitudes were performed in order to analyze the outputs. The steady state thermodynamic properties obtained from the data of performed experiments are presented in Table 4.5 below.

Table 4.5: Experimental Thermodynamic Data Collected at Different Resistance Magnitudes

	Units	Run 1	Run 2	Run 3	Run 4
Resistance Magnitude	ohm	0.667	1.667	3.333	8.333
P1 (Left chamber inlet)	kPa	177.9	248.7	249.9	261.1
P2 (Left chamber outlet)	kPa	7.8	2.6	2.3	3.4
P3 (Right chamber inlet)	kPa	179.4	247.8	248.9	260.6
P4 (Right chamber outlet)	kPa	2.6	3.0	3.6	3.1
T1 (Left chamber inlet)	°C	71.5	75.2	75.9	71.0
T2 (Left chamber outlet)	°C	63.2	62.7	57.5	52.4
T3 (Right chamber inlet)	°C	70.4	75.7	76.2	74.5
T4 (Right chamber outlet)	°C	52.1	59.3	53.1	50.9
V dot (air)	m3/s	0.00205	0.00168	0.00168	0.00168

In the performance analysis of the FPLE at different resistance magnitudes, the atmospheric pressure of 101.325 kPa was added to the pressure value measurements shown in Table 4.5 since they represent the gauge pressure values. It should be also noted that the steady state thermodynamic properties of Run 1, resistance magnitude of 0.667 ohm (Table 4.5) were the same as the 90 °C of the second experiment set, where the independent variable was the inlet air temperature. This was because both of the experiments' design parameters were identical. Therefore, the excessive internal leakage was also the probable reason for the measurement of lower chamber pressure values and higher volumetric flow rates compared to the other three experiments with different resistance magnitudes. Based on the thermodynamic data (Table 4.5) and the voltage-time data at steady state, the performance analysis of the FPLE at different resistance magnitudes was performed. The performance summary of the experimental data is presented in Table 4.6. The FPLE achieved the maximum isentropic efficiency of 20.4% with the resistance magnitude of

8.333 ohm, producing actual expander work and electrical power of 43.67 W and 0.033 W, respectively.

Table 4.6: The FPLE Performance Summary at Different Resistance Magnitudes

	Units	Run 1	Run 2	Run 3	Run 4
Frequency	Hz	31.03	38.03	37.03	34.03
Average RMS Voltage	W	0.503	0.642	1.488	2.320
Electrical Power Output	W	1.133	0.231	0.134	0.033
Actual Expander Work	W	33.63	29.88	42.89	43.67
Isentropic Expander Work	W	210.13	211.13	211.73	213.98
Irreversibility	%	175.17	183.96	172.77	176.82
Isentropic Efficiency	%	16.0	14.2	20.3	20.4
Mechanical-Electrical Conversion Efficiency	%	3.4	0.8	0.3	0.1
Volumetric Efficiency	%	119.5	79.8	81.9	89.2

Figure 4.10 presents the average RMS voltage trend versus different load magnitudes. The average RMS voltage was observed to increase as the resistance magnitude increased. The maximum average RMS voltage was achieved as 2.320 V at the resistance magnitude of 8.333 ohm and it can be anticipated that further increase in the resistance magnitude, the higher the average RMS voltage. The electrical power, unlike the voltage trend, was observed to be decreasing as the load magnitude increased. The maximum electric power was achieved at the load magnitude of 0.667 ohm as 1.133 W. The Figure 4.11 demonstrates the frequency trend versus different resistance magnitudes. The FPLE showed the maximum frequency of 38.02 Hz for 1.667 ohm. The frequency showed an increasing and then decreasing trend with increasing resistance.

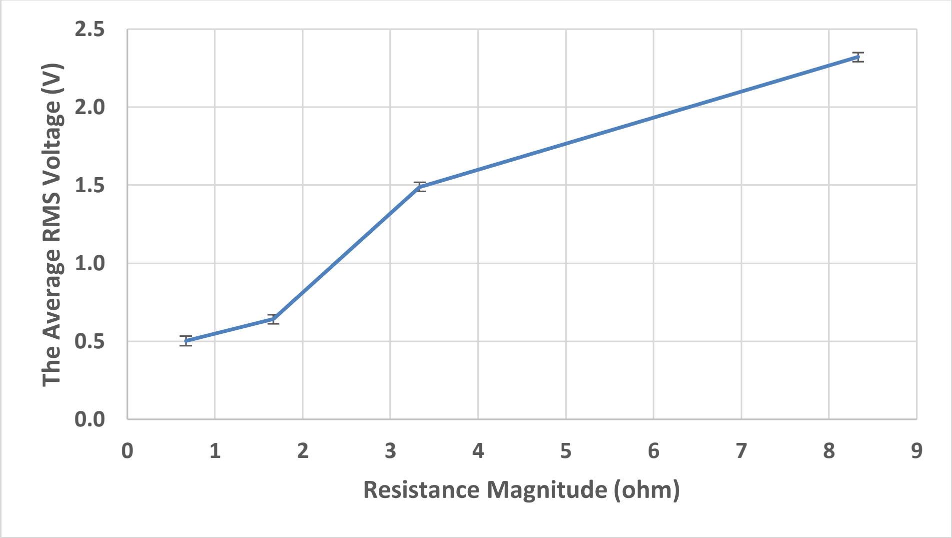

Figure 4.10: The Average RMS Voltages at Different Resistance Magnitudes

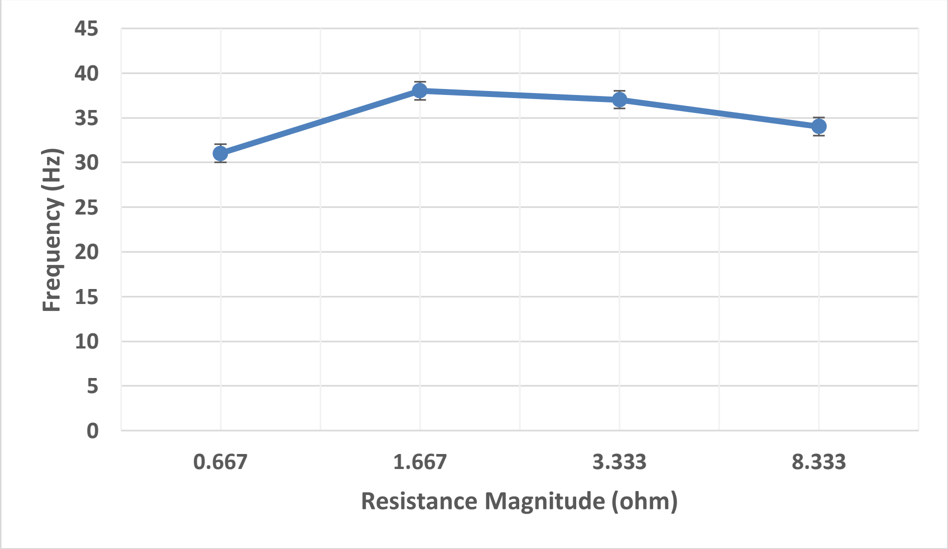

Figure 4.11: Variation of Expander Frequency for Different Resistance Magnitudes

Figure 4.12 presents the trends of the efficiencies at different load magnitudes. The results of the isentropic efficiency of the FPLE ranged between 14.2% and 20.4%. The maximum electrical power of 1.133 W was produced at 0.667 ohm when the FPLE had an isentropic efficiency of 16.0% with the mechanical-electrical conversion efficiency as 3.4%. As the resistance magnitude increased, the mechanical-electrical conversion efficiency significantly decreased. This led to lower electrical power at the higher resistance magnitudes even though the isentropic efficiency increased. At 0.667 ohm and 1.667 ohm, the isentropic efficiency did not change significantly, remaining within the propagation of error. Increasing the resistance magnitude from 1.667 ohm to 3.333 ohm resulted in an increase in the isentropic efficiency, achieving 20.3%. As the load was further increased from 3.333 ohm to 8.333 ohm, the expander reached the peak value of isentropic efficiency, 20.4%. The peak value of the volumetric efficiency was observed at the resistance magnitude of 0.667 ohm as 119.5%, then, it decreased to 79.8% for 1.667 ohm. The reason behind the peak volumetric efficiency of 119.5% can be connected to the possible excessive internal leakages taking place at the resistance magnitude of 0.667 ohm. As the internal leakage increased, more air was supplied to the system. This will lead to an increase in the volumetric flow rate and the volumetric efficiency. From 1.667 ohm to 3.333 ohm and then to 8.333 ohm, the volumetric efficiency had a tendency to increase, achieving 79.8%, 81.9% and 89.2%, respectively. From this trend, it can be anticipated that higher volumetric efficiencies than 89.2% can be achieved at even higher resistance magnitudes.

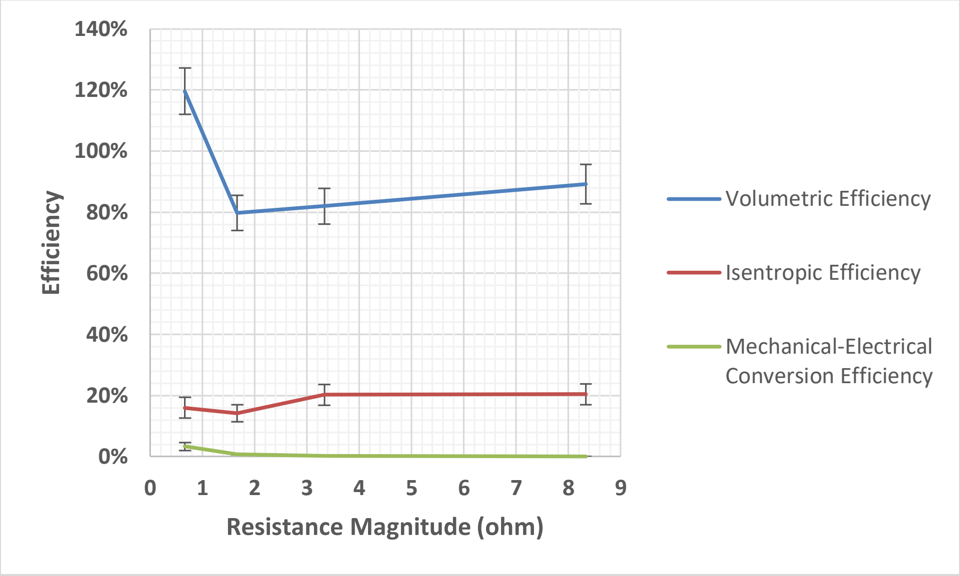

Figure 4.12: Efficiencies at Different Resistance Magnitudes

Figure 4.13 below displays the trends of the actual expander work and the irreversibility of the FPLE under different loads. The FPLE achieved the maximum actual expander work of 43.67 W in the Run 4 with the resistance magnitude of 8.333 ohm. From 0.667 ohm to 1.667 ohm, a decrease in the actual expander work was observed from 33.63 W to 29.88 W. Thereafter, from 1.667 ohm to 8.333 ohm, the actual expander work had a tendency to increase as the resistance magnitude increased; indicating that with further increase in the resistance magnitude, the actual expander work is likely to increase. The maximum irreversibility was observed as 183.96 W at the resistance magnitude of 1.667 ohm. Apart from that, no significant change was obtained in terms of irreversibility as the resistance magnitude increased.

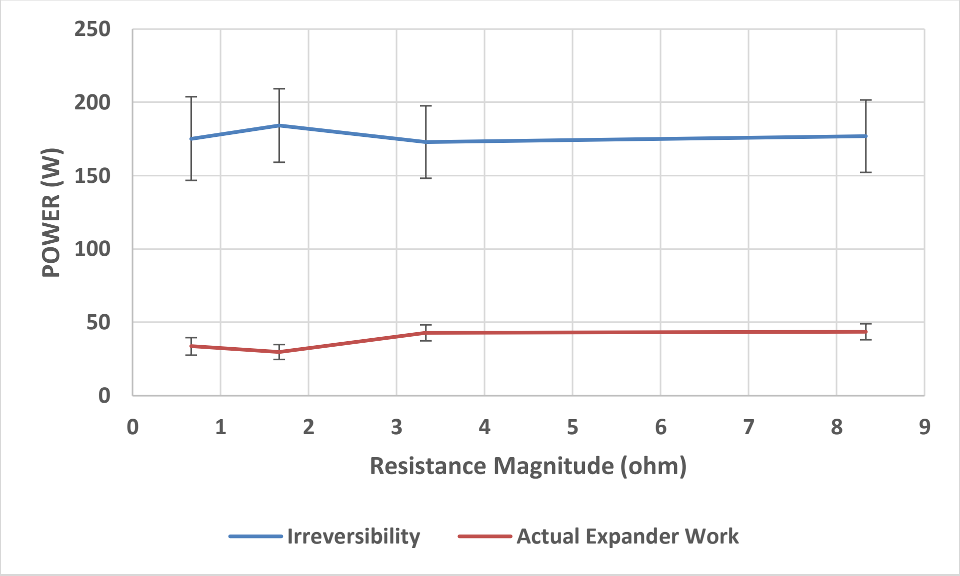

Figure 4.13: Actual Expander Work and Irreversibility Variations in Different Resistance Magnitudes

5 Conclusion

The previous design of the Free-Piston Linear expander (FPLE) was modified and the long-term steady state operation of the FPLE was successfully achieved. Three different sets of experiments were performed in order to analyze the performance of the FPLE with varying inlet air pressure, inlet air temperature, and resistance magnitude.

The frequency output of the FPLE had a tendency to increase as the inlet air pressure increased while increasing the inlet air temperature resulted in the decrease of the frequency. At the different resistance magnitudes, the frequency reached its peak value of 38.03 Hz. The maximum frequency in all the experiments was achieved as 44.01 Hz at an inlet air pressure and temperature, and the resistance magnitude of 551.6 kPa, 90 °C, and 0.667 ohm, respectively. It can be concluded from the trends that the frequency will likely increase at even higher inlet air pressures and even lower temperatures at a load magnitude of 1.667 ohm.

The FPLE produced the maximum average RMS voltage of 2.320 V at the inlet air pressure, inlet air temperature and the resistance magnitude of 413.7 kPa, 90 °C, and 8.333 ohm, respectively. It can be anticipated from the trends that the voltage is likely to increase at even higher inlet air pressures and resistance magnitudes with an optimum inlet air temperature of 60 °C. Electrical power output had similar trends to the RMS voltage with the only difference being that increasing the resistance magnitude significantly decreased the electrical power production.

The results showed that the maximum isentropic efficiency of the FPLE was achieved as 21.5%, producing maximum actual expander work and maximum electrical power of 75.13 W and 3.302 W, respectively. The maximum isentropic efficiency, at the different inlet air temperature experiments, was observed at the inlet air temperature of 80 °C. It can be concluded from the trends that the isentropic efficiency results remained within the propagation of error with the variation of resistance magnitudes. The mechanical-electrical conversion efficiency results ranged between 0.1%-7.1%, clearly indicating the cause of the large differences between the actual expander work and the electrical power output.

Volumetric efficiency reached its optimum point at the inlet air pressure of 482.6 kPa during the different inlet air pressure experiments. Varying the inlet air temperature did not significantly (within the propagation of error) change the volumetric efficiency, except for 90 °C. A relatively high volumetric efficiency was observed for 90 °C and 0.667 ohm. The most probable reason was an excessive internal leakage occurring between the piston O-rings and the cylinder walls. The measurements of relatively low chamber inlet pressures and high volumetric flow rates at these 90 °C and 0.667 ohm experiments also supported this hypothesis.

Actual expander work of the FPLE increased as the inlet air pressure increased, reaching its maximum value at the inlet air pressure of 551.6 kPa. Increasing the resistance magnitude from 1.667 ohm up to 8.333 ohm also resulted in higher actual expander work outputs. It can be concluded that the actual expander work will likely be higher at higher inlet air pressures and resistance magnitudes, noting that the optimum temperature for actual expander work was 80 °C. Irreversibility, on the other hand, showed a tendency to increase as the inlet air pressure increased, and to decrease as the inlet air temperature increased. However, the changes in the irreversibility at different inlet air temperatures were within the propagation of error. Varying the resistance magnitude did not significantly change the irreversibility.

In the literature, turbines, scroll expanders, screw expanders, rotary vane expanders, gerotor, reciprocating piston expanders, and rotary piston expanders were found to achieve isentropic efficiencies of up to 85%, 50-89%, up to 76%, 23-73%, up to 85%, up to 70%, and 28-77%, respectively. In this study, the maximum isentropic efficiency of the FPLE was 21.5%. It should be noted this was the first iteration of this FPLE design.

6 Future Work

The following options are recommended in order to improve the performance of the current design:

- Further research and parametric study should be conducted on the separation of losses to gain further insight into the performance of the FPLE.
- Further study is needed to ensure better vibration damping during the expander's operation.
- Further research should be conducted to improve the material of O-ring on the purpose of providing better sealing and reducing the friction between the O-rings and the cylinder wall.
- Further study can be performed in order to investigate the effect of varying the expansion ratio on the performance of the FPLE.
- Mechanical-electrical conversion mechanism should be improved in order to reduce the difference between the actual expander work output and the electrical power produced. Therefore, further research can be conducted on the magnet selection, coil wiring, and the electrical circuit design.

References

1 Spielvogel, J. (2014). The Industrial Revolution and Its Impact on European Society. In *Western Civilization: Volume II: Since 1500* (9th ed., Vol. II, pp. 596-623). Stamford: Cengage Learning.

2 World Energy Outlook 2013. (2013). Paris: International Energy Agency, 708 pp.

3 Sonntag, R. E., Borgnakke, C., & Wylen, G. J. (2003). *Fundamentals of Thermodynamics* (6th ed.). New York: Wiley. 814 pp.

4 Annual Energy Review 2011. (2012). Washington, DC: U.S. Energy Information Administration, p. 37.

5 Beér, J. M. (2007). High efficiency electric power generation: The environmental role. *Progress in Energy and Combustion Science, 33*(2), 107-134.

6 Bonar, H. (2002). *U.S. Patent No. 6,484,498*. Washington, DC: U.S. Patent and Trademark Office.

7 Imran, M., Usman, M., Park, B., & Lee, D. (2016). Volumetric expanders for low grade heat and waste heat recovery applications. *Renewable and Sustainable Energy Reviews, 57*, 1090-1109.

8 Avadhanula, V. K. (2015). *Evaluation and parametric modeling of 50 kW organic rankine cycle for waste heat recovery from rural Alaska diesel generator power plants* (Doctoral Dissertation). University of Alaska Fairbanks. 224 pp.

9 Kalina, A. I. (1982). *U.S. Patent No. 4,346,561*. Washington, DC: U.S. Patent and Trademark Office.

10 Matsuda, K. (2014). Low heat power generation system. *Applied Thermal Engineering, 70*(2), 1056-1061.

11 Marston, C.H. 1990. Parametric analysis of the Kalina cycle. *Journal of Engineering for Gas Turbines and Power, 112*(1), 107–116.

12 Corman, J.C., Bjorge, R.W., & Kalina, A. (1995). Kalina cycle looks good for combined cycle generation. MPS Review 19–22.

13 Hettiarachchi, H. D., Golubovic, M., Worek, W. M., & Ikegami, Y. (2007). The Performance of the Kalina Cycle System 11(KCS-11) With Low-Temperature Heat Sources. *Journal of Energy Resources Technology, 129*(3), 243.

14 Park, Y. M. & Sonntag, R. E. (1990). A preliminary study of the kalina power cycle in connection with a combined cycle system. *International Journal of Energy Research, 14*(2), 153-162.

15 Harada, K. J. (2010). *Development of a Small Scale Scroll Expander* (Master's Thesis). Oregon State University. 142 pp.

16 Quoilin, S. (2007). *Experimental Study and Modeling of a Low Temperature Rankine Cycle for Small Scale Cogeneration* (Master's Thesis). University of Liege. 129 pp.

17 Kinnaly, E. B. & Nuszkowski, J. (2015). Volumetric Rotary Expansion Machines – A Review. Jacksonville: University of North Florida.

18 Fraas, A. P. (1982). Engineering evaluation of energy systems. New York: McGraw-Hill. 702 pp.

19 Yang, J. L., Ma, Y. T., Li, M. X., & Guan, H. Q. (2005). Exergy analysis of transcritical carbon dioxide refrigeration cycle with an expander. *Energy, 30*(7), 1162-1175.

20 Chen, Y., Lundqvist, P., Johansson, A., & Platell, P. (2006). A comparative study of the carbon dioxide transcritical power cycle compared with an organic rankine cycle with R123 as working fluid in waste heat recovery. *Applied Thermal Engineering, 26*(17-18), 2142-2147.

21 Baek, J., Groll, E., & Lawless, P. (2005). Piston-cylinder work producing expansion device in a transcritical carbon dioxide cycle. Part I: Experimental investigation. *International Journal of Refrigeration, 28*(2), 141-151.

22 Kongtragool, B. & Wongwises, S. (2007). Performance of low-temperature differential Stirling engines. *Renewable Energy, 32*(4), 547-566

23 Çengel, Y. A. & Boles, M. A. (2006). *Thermodynamics: An engineering approach* (5th ed.). Boston: McGraw-Hill. 963 pp.

24 Tarique, M. A. (2011). *Experimental investigation of scroll based organic Rankine systems* (Master's Thesis). University of Ontario Institute of Technology. 186 pp.

25 Çinar, C. & Karabulut, H. (2005). Manufacturing and testing of a gamma type Stirling engine. *Renewable Energy, 30*(1), 57-66.

26 Thombare, D. & Verma, S. (2008). Technological development in the Stirling cycle engines. *Renewable and Sustainable Energy Reviews, 12*(1), 1-38.

27 Yang, B., Ahuja, H., & Tran, T. (2008). Review Article: Thermoelectric Technology Assessment: Application to Air Conditioning and Refrigeration. *HVAC&R Res. UHVC HVAC&R Research, 14*(5), 635-653.

28 Oralli, E. (2010). *Conversion of a scroll compressor to an expander for organic Rankine cycle: Modeling and analysis* (Master's thesis). University of Ontario Institute of Technology. 162 pp.

29 Kumar, S., Heister, S. D., Xu, X., Salvador, J. R., & Meisner, G. P. (2013). Thermoelectric Generators for Automotive Waste Heat Recovery Systems Part I: Numerical Modeling and Baseline Model Analysis. *Journal of Electronic Materials, 42*(4), 665-674.

30 Aphornratana, S. & Sriveerakul, T. (2010). Analysis of a combined Rankine–vapour–compression refrigeration cycle. *Energy Conversion and Management, 51*(12), 2557-2564.

31 Lemort, V., Quoilin, S., Cuevas, C., & Lebrun, J. (2009). Testing and modeling a scroll expander integrated into an Organic Rankine Cycle. *Applied Thermal Engineering, 29*(14-15), 3094-3102.

32 Desideri, A., Gusev, S., Broek, M. V., Lemort, V., & Quoilin, S. (2016). Experimental comparison of organic fluids for low temperature ORC (organic Rankine cycle) systems for waste heat recovery applications. *Energy, 97*, 460-469.

33 Hung, T., Shai, T., & Wang, S. (1997). A review of organic rankine cycles (ORCs) for the recovery of low-grade waste heat. *Energy, 22*(7), 661-667.

34 Larjola, J. (1995). Electricity from industrial waste heat using high-speed organic Rankine cycle (ORC). *International Journal of Production Economics, 41*(1-3), 227-235.

35 Tchanche, B. F., Lambrinos, G., Frangoudakis, A., & Papadakis, G. (2011). Low-grade heat conversion into power using organic Rankine cycles – A review of various applications. *Renewable and Sustainable Energy Reviews, 15*(8), 3963-3979.

36 Manolakos, D., Kosmadakis, G., Kyritsis, S., & Papadakis, G. (2009). On site experimental evaluation of a low-temperature solar organic Rankine cycle system for RO desalination. *Solar Energy, 83*(5), 646-656.

37 Quoilin, S., Orosz, M., Hemond, H., & Lemort, V. (2011). Performance and design optimization of a low-cost solar organic Rankine cycle for remote power generation. *Solar Energy, 85*(5), 955-966.

38 Hettiarachchi, H. M., Golubovic, M., Worek, W. M., & Ikegami, Y. (2007). Optimum design criteria for an Organic Rankine cycle using low-temperature geothermal heat sources. *Energy, 32*(9), 1698-1706.

39 Heberle, F. & Brüggemann, D. (2015). Thermo-Economic Evaluation of Organic Rankine Cycles for Geothermal Power Generation Using Zeotropic Mixtures. *Energies, 8*(3), 2097-2124.

40 Barbier, E. (2002). Geothermal energy technology and current status: An overview. *Renewable and Sustainable Energy Reviews, 6*(1-2), 3-65.

41 Engin, T. & Ari, V. (2005). Energy auditing and recovery for dry type cement rotary kiln systems—A case study. *Energy Conversion and Management, 46*(4), 551-562.

42 Saleh, B., Koglbauer, G., Wendland, M., & Fischer, J. (2007). Working fluids for low-temperature organic Rankine cycles. *Energy, 32*(7), 1210-1221

43 Wang, E., Zhang, H., Fan, B., Ouyang, M., Zhao, Y., & Mu, Q. (2011). Study of working fluid selection of organic Rankine cycle (ORC) for engine waste heat recovery. *Energy, 36*(5), 3406-3418.

44 Quoilin, S., Declaye, S., Legros, A., Guillaume, L., & Lemort, V. (2012). Working fluid selection and operating maps for organic Rankine cycle expansion machines. In: Proceeding of the International Compressor Engineering Conference, Purdue paper 1546.

45 Tchanche, B. F., Papadakis, G., Lambrinos, G., & Frangoudakis, A. (2009). Fluid selection for a low-temperature solar organic Rankine cycle. *Applied Thermal Engineering, 29*(11-12), 2468-2476.

46 Hung, T. (2001). Waste heat recovery of organic Rankine cycle using dry fluids. *Energy Conversion and Management, 42*(5), 539-553.

47 Peterson, R. B., Wang, H., & Herron, T. (2008). Performance of a small-scale regenerative Rankine power cycle employing a scroll expander. *Proceedings of the Institution of Mechanical Engineers, Part A: Journal of Power and Energy, 222*(3), 271-282.

48 U.S. Department of Energy. (2008). Waste heat recovery: technology and opportunities in U.S. industry. *Tech. Report; U.S. Department of Energy Industrial Technologies Program*, p. 7.

49 Manolakos, D., Papadakis, G., Kyritsis, S., & Bouzianas, K. (2007). Experimental evaluation of an autonomous low-temperature solar Rankine cycle system for reverse osmosis desalination. *Desalination, 203*(1-3), 366-374.

50 Elgin, A. (2015). *Development of an Expander for Low Grade Thermal Energy Conversion Using Organic Rankine Cycle: Modeling and Testing* (Master's Thesis). San Diego State University. 93 pp.

51 Persson, J. & Sohlenius, G. (1990). Performance Evaluation of Fluid Machinery During Conceptual Design. *CIRP Annals - Manufacturing Technology, 39*(1), 137-140.

52 Yamamoto, T., Furuhata, T., Arai, N., & Mori, K. (2001). Design and testing of the Organic Rankine Cycle. *Energy, 26*(3), 239-251.

53 Yagoub, W., Doherty, P., & Riffat, S. (2006). Solar energy-gas driven micro-CHP system for an office building. *Applied Thermal Engineering, 26*(14-15), 1604-1610.

54 Kang, S. H. (2012). Design and experimental study of ORC (organic Rankine cycle) and radial turbine using R245fa working fluid. *Energy, 41*(1), 514-524.

55 Fukuta, M., Yanagisawa, T., Kosuda, O., & Ogi, Y. (2006). Performance of scroll expander for CO2 refrigeration cycle. In: Proceedings of the International Compressor Engineering Conference, Purdue paper 1768.

56 Xiaojun, G., Liansheng, L., Yuanyang, Z., & Pengcheng, S. (2004). Research on a Scroll Expander Used for Recovering Work in a Fuel Cell. *International Journal of Thermodynamics, 7*(1), 1-8.

57 Lemort, V., Quoilin, S., Cuevas, C., & Lebrun, J. (2009). Testing and modeling a scroll expander integrated into an Organic Rankine Cycle. *Applied Thermal Engineering, 29*(14-15), 3094-3102.

58 Mathias, J. A., Johnston, J. R., Cao, J., Priedeman, D. K., & Christensen, R. N. (2009). Experimental Testing of Gerotor and Scroll Expanders Used in, and Energetic and Exergetic Modeling of, an Organic Rankine Cycle. *Journal of Energy Resources Technology J. Energy Resour. Technol., 131*(1), 012201-1-012201-9.

59 Sprankle, R. S. (1973). *U.S. Patent No. 3,751,673*. Washington, DC: U.S. Patent and Trademark Office.

60 Lu, Y., He, W., Wu, Y., Ji, W., Ma, C., & Guo, H. (2013). Performance study on compressed air refrigeration system based on single screw expander. Energy, 55, 762-768.

61 Smith, I. K., Stosic, N., & Kovacevic, A. (2005). Screw Expanders Increase Output and Decrease the Cost of Geothermal Binary Power Plant Systems. London: City University London.

62 Smith, I. K., Stosic, N., & Kovacevic, A. (1999). Power Recovery from Low Cost Two-Phase Expanders. London: City University London.

63 Bao, J. & Zhao, L. (2013). A review of working fluid and expander selections for organic Rankine cycle. *Renewable and Sustainable Energy Reviews, 24*, 325-342.

64 Smith, I. K., Stosic, N., Aldis, C. A., & Kovacevic, A. (2000). Twin Screw Two-Phase Expanders in Large Chiller Units. London: City University London.

65 Tahir, M. B. M., Yamada, N., & Hoshino, T. (2010). Efficiency of Compact Organic Rankine Cycle System with Rotary-Vane-Type Expander for Low-Temperature Waste Heat Recovery. *International Journal of Environmental Science and Engineering, 2*(1), 11-16.

66 Badr, O., O'Callaghan, P., Hussein, M., & Probert, S. (1984). Multi-vane expanders as prime movers for low-grade energy organic Rankine-cycle engines. *Applied Energy, 16*(2), 129-146.

67 Badr, O., Probert, S., & O'Callaghan, P. (1985). Performances of multi-vane expanders. *Applied Energy, 20*(3), 207-234.

68 Yang, B., Peng, X., He, Z., Guo, B., & Xing, Z. (2009). Experimental investigation on the internal working process of a CO2 rotary vane expander. *Applied Thermal Engineering, 29*(11-12), 2289-2296.

69 Mathias, J. A., Johnston, J. R., Cao, J., Priedeman, D. K., & Christensen, R. N. (2009). Experimental Testing of Gerotor and Scroll Expanders Used in, and Energetic and Exergetic Modeling of, an Organic Rankine Cycle. *Journal of Energy Resources Technology, 131*(1), 012201-1-012201-9.

70 Zhang, B., Peng, X., He, Z., Xing, Z., & Shu, P. (2007). Development of a double acting free piston expander for power recovery in transcritical CO2 cycle. *Applied Thermal Engineering, 27*(8-9), 1629-1636.

71 Baek, J., Groll, E., & Lawless, P. (2005). Piston-cylinder work producing expansion device in a transcritical carbon dioxide cycle. Part I: Experimental investigation. *International Journal of Refrigeration, 28*(2), 141-151.

72 Glavatskaya, Y., Podevin, P., Lemort, V., Shonda, O., & Descombes, G. (2012). Reciprocating Expander for an Exhaust Heat Recovery Rankine Cycle for a Passenger Car Application. *Energies, 5*(12), 1751-1765.

73 Haiqing, G., Yitai, M., & Minxia, L. (2006). Some design features of CO2 swing piston expander. *Applied Thermal Engineering, 26*(2-3), 237-243.

74 Wang, X., Zhao, L., Wang, J., Zhang, W., Zhao, X., & Wu, W. (2010). Performance evaluation of a low-temperature solar Rankine cycle system utilizing R245fa. *Solar Energy, 84*(3), 353-364.

75 Jiang, Y., Ma, Y., Fu, L., & Li, M. (2013). Some design features of CO2 two-rolling piston expander. *Energy, 55*, 916-924.

76 Hu, J., Li, M., Zhao, L., Xia, B., & Ma, Y. (2015). Improvement and experimental research of CO2 two-rolling piston expander. *Energy, 93*, 2199-2207.

77 Hawn, M., Johanning, M., Parker, K., & Clarkson, B. (2013). Design and Manufacture of a Free Piston Linear Alternator. Jacksonville: University of North Florida.

78 Nuszkowski, J., Harris, A., & Eason, P. (2012). Assessment of “the Expander,” an Apparatus and Method for converting Thermal to Electrical Energy. Jacksonville: University of North Florida.

79 Wang, Y., Chen, L., Jia, B., & Roskilly, A. P. (2017). Experimental study of the operation characteristics of an air-driven free-piston linear expander. Applied Energy, 195, 93-99.

80 Zhang, B., Peng, X., He, Z., Xing, Z., & Shu, P. (2007). Development of a double acting free piston expander for power recovery in transcritical CO2 cycle. Applied Thermal Engineering, 27(8-9), 1629-1636.

81 Preetham, B. & Weiss, L. (2016). Investigations of a new free piston expander engine cycle. Energy, 106, 535-545.

82 Champagne, C. & Weiss, L. (2013). Performance analysis of a miniature free piston expander for waste heat energy harvesting. Energy Conversion and Management, 76, 883-892.

83 Li, G., Zhang, H., Yang, F., Song, S., Chang, Y., Yu, F., Wang, J., & Yao, B. (2016). Preliminary Development of a Free Piston Expander–Linear Generator for Small-Scale Organic Rankine Cycle (ORC) Waste Heat Recovery System. Energies, 9(4), 300.

84 McMaster-Carr. Retrieved June 23, 2017, from
https://www.mcmaster.com/#9657k342/=18ht3yy

85 OMEGA AHP Series - Instruction Sheet. (2017). Retrieved June 23, 2017, from
https://www.omega.com/manuals/manualpdf/M2157.pdf

86 McMaster-Carr. Retrieved June 23, 2017, from
https://www.mcmaster.com/#5556k32/=18kwuaq

87 EGT Temperature Sensors w 90° Bend & 1/8" NPT Compression Fittings for Exhaust. Retrieved June 23, 2017, from
http://www.ebay.com/itm/EGT-Temperature-Sensors-w-90-Bend-1-8-NPT-Compression-Fittings-for-Exhaust-/171999724386

88 Replacement Gauge for Husky Air Compressor. Retrieved June 23, 2017, from
http://www.ebay.com/itm/Replacement-Gauge-for-Husky-Air-Compressor-/122474266976

89 MPX5700GP. Retrieved June 23, 2017, from
https://www.digikey.com/product-detail/en/nxp-usa-inc/MPX5700GP/MPX5700GP-ND/464063

90 7520 / 7530 Series. Retrieved June 23, 2017, from
https://kinginstrumentco.com/wp-content/uploads/2016/11/King-Catalog-2016-2017-7520-7530.pdf

91 Appendix A - Specifications. Retrieved June 23, 2017, from
https://labjack.com/support/datasheets/u12/appendix-a

92 LibreTexts. (2017, March 14). Propagation of Error. Retrieved June 22, 2017, from
https://chem.libretexts.org/Core/Analytical_Chemistry/Quantifying_Nature/Significant_Digits/Propagation_of_Error

APPENDIX A

Table A.1: Standard Deviation Results of the Calculated Parameters for Experimental Set 1

STANDARD DEVIATION					
INDEPENDENT VARIABLE - Inlet Air Pressure					
	Run 1	Run 2	Run 3	Run 4	Run 5
Frequency (Hz)	1	1	1	1	4
Average RMS Voltage (V)	0.03	0.03	0.03	0.03	0.045
Electrical Power Output (W)	0.39	0.39	0.39	0.39	0.48
Actual Expander Work (W)	4.01	4.80	5.59	6.82	7.28
Isentropic Expander Work (W)	18.52	21.57	24.12	27.83	28.31
Irreversibility (W)	18.75	22.29	25.64	31.08	31.66
Isentropic Efficiency (-)	0.04	0.04	0.03	0.03	0.03
Mechanical-Electrical Conversion Efficiency (-)	0.02	0.01	0.01	0.01	0.01
Volumetric Efficiency (-)	0.07	0.06	0.06	0.06	0.10

Table A.2: Standard Deviation Results of the Calculated Parameters for Experimental Set 2

STANDARD DEVIATION					
INDEPENDENT VARIABLE - Inlet Air Temperature					
	Run 1	Run 2	Run 3	Run 4	Run 5
Frequency (Hz)	1	1	1	1	1
Average RMS Voltage (V)	0.03	0.03	0.03	0.03	0.03
Electrical Power Output (W)	0.39	0.39	0.39	0.39	0.39
Actual Expander Work (W)	4.99	5.12	5.09	5.24	5.86
Isentropic Expander Work (W)	21.53	22.08	22.49	22.84	26.49
Irreversibility (W)	25.06	24.84	24.79	24.66	28.41
Isentropic Efficiency (-)	0.03	0.03	0.03	0.03	0.03
Mechanical-Electrical Conversion Efficiency (-)	0.02	0.02	0.01	0.01	0.01
Volumetric Efficiency (-)	0.06	0.06	0.06	0.06	0.08

Table A.3: Standard Deviation Results of the Calculated Parameters for Experimental Set 3

STANDARD DEVIATION				
INDEPENDENT VARIABLE - Resistance Magnitude				
	Run 1	Run 2	Run 3	Run 4
Frequency (Hz)	1	1	1	1
Average RMS Voltage (V)	0.03	0.03	0.03	0.03
Electrical Power Output (W)	0.39	0.062	0.016	0.002
Actual Expander Work (W)	5.86	4.97	5.37	5.40
Isentropic Expander Work (W)	26.49	23.18	23.20	22.97
Irreversibility (W)	28.41	25.03	24.65	24.68
Isentropic Efficiency (-)	0.03	0.03	0.03	0.03
Mechanical-Electrical Conversion Efficiency (-)	0.013	0.0025	0.0005	0.0001
Volumetric Efficiency (-)	0.08	0.06	0.06	0.06